J. Fluid Mech. (1988), *vol.* 187, *pp.* 61–98
Printed in Great Britain

Direct simulation of a turbulent boundary layer up to $R_\theta = 1410$

By PHILIPPE R. SPALART
NASA Ames Research Center, Moffett Field, CA 94035, USA

(Received 12 December 1986 and in revised form 13 May 1987)

The turbulent boundary layer on a flat plate, with zero pressure gradient, is simulated numerically at four stations between $R_\theta = 225$ and $R_\theta = 1410$. The three-dimensional time-dependent Navier–Stokes equations are solved using a spectral method with up to about 10^7 grid points. Periodic spanwise and streamwise conditions are applied, and a multiple-scale procedure is applied to approximate the slow streamwise growth of the boundary layer. The flow is studied, primarily, from a statistical point of view. The solutions are compared with experimental results. The scaling of the mean and turbulent quantities with Reynolds number is compared with accepted laws, and the significant deviations are documented. The turbulence at the highest Reynolds number is studied in detail. The spectra are compared with various theoretical models. Reynolds-stress budget data are provided for turbulence-model testing.

1. Introduction

The behaviour of turbulent boundary layers is far from being fully understood, and accurate predictions are difficult except in the simplest cases. Scaling laws have been proposed and validated by measurements, e.g. the 'law of the wall' and the 'defect law'. Other laws, such as Kolmogorov's, may apply but are not specific to wall-bounded flows. These laws express our understanding of the mechanics of turbulent flows. They are also constantly used to extrapolate results from one Reynolds number to the other. The Reynolds numbers encountered in practical applications are much higher than can be reached in laboratory experiments or, *a fortiori*, in direct numerical simulations.

The theoretical foundation of the laws is often fragile; for instance several interpretations have been given for the 'log law'. This is troublesome when one attempts to generalize the laws, either to more complex flows (e.g. pressure gradients) or to other quantities (e.g. higher statistical moments). The different interpretations, which agree in the simple case, may conflict in the general case. Often the available measurements are not accurate enough to indicate which theory is correct, and there is no consensus. Furthermore, the theories are usually unable to predict the value of the universal constants (e.g. the Kármán and Kolmogorov constants). For the theory of turbulent boundary layers, see in particular Coles (1956) and Townsend (1956, 1976).

Another area of controversy is the behaviour of turbulent flows at low Reynolds numbers. The flow is turbulent in the sense that the fluctuations have a significant energy and have a strong effect on the mean flow through the Reynolds stresses they generate. On the other hand the range of scales is not sufficient for many widely-used theoretical arguments, which are based on the separation of large and small scales,

to apply. Typical examples are the inertial range in the spectrum of small-scale turbulence and the log layer near a wall; both properties vanish when the Reynolds number is too low. Unfortunately, all direct numerical simulations to date fall into the range of 'low-Reynolds-number turbulence'. This makes the interpretation of the results delicate; it is often hard to tell whether a result is close to the asymptotic high-Reynolds-number value, or even whether a finite asymptotic value exists. One needs to distinguish between 'Reynolds-number effects' and 'low-Reynolds-number effects'. In an effort to achieve this distinction in the present study, particular care was taken to prevent spurious numerical effects. The simulations also cover a rather wide range of Reynolds numbers (a factor of 4), and the results suggest that in the $R_\theta = 1410$ flow the low-Reynolds-number effects are weak. For low-Reynolds-number effects see in particular Coles (1962), Head & Bandyopadhyay (1981), Purtell, Klebanoff & Buckley (1981), Murlis, Tsai & Bradshaw (1982) and Erm, Smits & Joubert (1985).

In addition to theoretical results like the scaling laws, fundamental turbulence research is expected to provide quantitative results for the calibration of turbulence models. These models are needed for the prediction of practical flows; their present accuracy leaves much room for improvement. From an accurate direct simulation, one can extract all the quantities that are involved in a turbulence model of any complexity. This provides a complete test of the model and leads to suggestions about how to improve it. Here one is making the assumption that an extrapolation is possible not only to higher Reynolds numbers, but also to more complex geometries. The present study focuses on conventional, statistical measures of turbulence. The modern concepts of coherent structures in turbulence are not ignored, but the open questions regarding the behaviour of quantities as simple as the mean velocity and the Reynolds stresses are urgent both from a theoretical point of view (scaling laws) and from a practical point of view (turbulence models). They are also more likely to have durable answers.

Direct and large-eddy simulations of turbulence were reviewed by Rogallo & Moin (1984). In the field of wall-bounded flows, Deardoff (1970) and Schumann (1975) studied turbulent channel flow by large-eddy simulation, without resolving the viscous wall region. Moin & Kim (1982) did a large-eddy simulation and could resolve the wall region; they obtained close agreement with the well-known law of the wall. Moser & Moin (1984) performed a direct simulation of (curved) turbulent channel flow. In contrast to large-eddy simulations, direct simulations do not include modelling of the eddies smaller than the grid spacing. This limits them to lower Reynolds numbers, but the results are thought to be more reliable, especially close to the wall (Moser & Moin 1984). See also the work by Orszag's group (Pelz *et al.* 1985). These studies did not emphasize the Reynolds-number dependence of the turbulent quantities and relied heavily on wall scaling (based on the friction velocity u_τ and the kinematic viscosity ν) to present the results and compare them with experiments.

An earlier version of the method used here was applied to equilibrium boundary layers with pressure gradients by Spalart & Leonard (1985) and to sink-flow boundary layers by Spalart (1986*b*). In both studies the flows were assumed, locally, to satisfy similarity properties both in the wall region (law of the wall) and in the outer region (defect law). These assumptions were involved in the multiple-scale approximation that accounted for the slow streamwise evolution of the flow. Self-similarity was assumed both for the mean velocity and for the Reynolds stresses. These assumptions are reasonable, but are strongly justified only in the case of the

sink flow. In fact when Spalart & Leonard compared simulations (with zero pressure gradient) at different Reynolds numbers, it was found that some of the scaling laws were not satisfied. Thus the study as a whole was inconsistent, in that the global behaviour of the flow negated the assumptions that were made locally. The deviations from the scaling laws were especially striking near the wall, where the terms which depend on the similarity assumptions are very weak. Therefore it was expected that even if these terms were altered to remove the inconsistency, the results would not change significantly and the deviations would remain.

This finding motivated a generalization of the approach and a systematic, controlled study of the Reynolds-number effects. The new approach makes no assumption about the behaviour of the dependent variables. The outer and inner lengthscales δ and ν/u_τ are still used to define a transformation of the independent variable in the direction normal to the wall, but as this is a much weaker assumption it can only have an indirect effect on the results. The procedure will be described in §2.3. Although it has much in common with the procedures used by Spalart & Leonard (1985) and Spalart (1986*b*) a self-contained account of the method will be given.

The numerical method was described in detail by Spalart (1986*a*). It is fully spectral in space, based on Fourier series in the directions parallel to the plate and an exponential mapping with Jacobi polynomials in the normal, semi-infinite direction. The time integration is second-order accurate and hybrid; it uses a low-storage Runge–Kutta scheme (Wray 1987) for the transport term and the Crank–Nicolson scheme for the Stokes terms. If Reynolds-number effects are to be studied by numerical simulation, it is essential to ensure that the different cases are not run with (effectively) different resolution, which could induce spurious variations. A similar problem can occur in experiments, for instance if a probe of fixed size is used while an increase in the Reynolds number decreases the scales of the turbulence.

There are two aspects to the question of resolution. One is the size of the domain in the directions parallel to the wall (or equivalently the smallest wavenumber). It was decided to keep the ratio of these dimensions to the displacement thickness δ^* the same in all the simulations. Thus if there is an effect of the confinement of the flow inside a finite domain, the effect will be as independent of Reynolds number as possible. The displacement thickness is an appropriate macroscale of the flow and, with the present method, happens to be easier to control than the boundary-layer thickness δ or the momentum thickness θ. The lengthscale y_0 of the exponential mapping (Spalart 1986*a*) is also kept at a constant multiple of δ^*. The other aspect is of course the grid spacing (or equivalently the largest wavenumber). In this case the wall region is the most sensitive and it was decided that the grid spacing should be fixed, in wall units. Thus the effects of numerical truncation will be as independent of Reynolds number as possible.

2. Governing equations

2.1. *Multiple-scale approximation*

The overall goal is to obtain a set of equations which, when solved with periodic conditions in the streamwise (x) direction, can provide a good approximation to the local state of a boundary layer that has a slow spatial development. The incentives to use periodic conditions are both numerical (the high accuracy of Fourier series) and physical (no need to provide turbulent inflow conditions, improved statistical

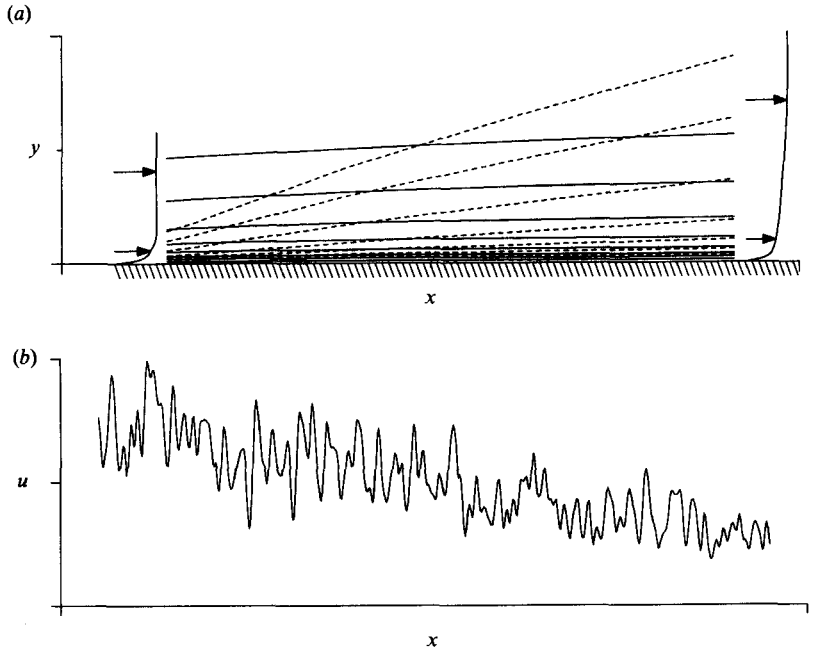

FIGURE 1. Sketch of a spatially-developing boundary layer. (*a*) Geometry. →, velocity vectors; ——, streamlines; – – –, coordinate lines. (*b*) Turbulent signal.

sample). The idea is to use the fact that both the thickness of the boundary layer and the energy level of the turbulence vary slowly as functions of x. The final product is a set of small 'growth terms' that are added to the usual Navier–Stokes equations.

Figure 1 (*a*) is a sketch of the flow, with the normal direction (y) enlarged about 10 times. The velocity profiles at two stations illustrate the thickening of the boundary layer. The solid lines represent streamlines of the mean velocity field, which are at a shallow angle to the wall. The dashed lines represent a coordinate system that is 'fitted' to the boundary layer. The periodic conditions will be applied along these lines. A new coordinate η (which is constant along a dashed line) replaces y as the normal coordinate; it is chosen so that the boundary-layer thickness and the viscous-sublayer thickness are independent of x. In the sink flow the coordinate lines were obvious: they were the rays converging into the sink. In the general case the choice is more arbitrary and will be discussed in §§2.2 and 2.3. In terms of geometry, the key quantity is the slope S of the coordinate lines. In the constant-pressure boundary layer, as indicated in figure 1 (*a*), S is positive and small, although larger than the slope of the streamlines.

The dependent variables also require a change of variables before periodic conditions are applied. Figure 1 (*b*) is a sketch of a turbulent velocity component, for instance u, *vs.* x (at fixed values of η, z and t). The signal displays fast, short-scale fluctuations as well as a slow variation of the mean and of the intensity of the fluctuations with x. This makes periodic conditions inadequate. However if one writes u as the combination

$$u(x,\eta,z,t) = U(x,\eta)+A(x,\eta)\,u_{\mathrm{p}}(x,\eta,z,t), \tag{1}$$

where U is the mean (over the spanwise direction z and time t) and the 'amplitude function' A is proportional to the r.m.s. of the fluctuations, then the normalized

signal u_p has zero mean and its r.m.s. is independent of x. This makes periodic conditions for u_p appear tolerable although not fully justified. They are not fully justified because the length- and timescales of the signal may vary with x, so that even u_p is not a truly homogeneous signal. However in a boundary layer, the variation of these scales is presumed to be slow and to have a weaker effect than the variation of the mean and r.m.s.

Differentiating (1) with respect to x yields

$$\frac{\partial u}{\partial x} = \frac{\partial U}{\partial x} + A\frac{\partial u_p}{\partial x} + \frac{\partial A}{\partial x}u_p. \tag{2}$$

Since the variation of U and A with x is assumed to be slow, the first and third terms appear as small corrections, 'slow derivatives', denoted by U_X and u_X. The second term, the usual or 'fast' derivative $\partial u_p/\partial x$, is denoted by u_x. The formulae for U_X and u_X will be discussed in §2.3.

2.2. *Short-scale analysis*

The short-scale analysis includes the transformation of the Navier–Stokes equations from the Cartesian system of coordinates (x, y, z) to the non-Cartesian system (x, η, z), the inclusion of the slow derivatives, and the Taylor expansion of the resulting equations. The metric coefficients S and T of the coordinate transformation are defined by

$$\begin{pmatrix} \mathrm{d}x \\ \mathrm{d}y \end{pmatrix} \equiv \begin{pmatrix} 1 & 0 \\ S & T \end{pmatrix} \begin{pmatrix} \mathrm{d}x \\ \mathrm{d}\eta \end{pmatrix}. \tag{3}$$

S has a clear physical meaning: it is the slope made by the new coordinate lines with the wall. The meanings of η and T are not as clear, since they depend on a normalization. In the end the normalization will be chosen so that, at the value of x being considered, η and y coincide, giving $T = 1$. Until then the identity $T_x = S_\eta$ will be used to express the results in terms of S as much as possible.

Let (u^*, v^*, w^*) be the Cartesian velocity components. The contravariant velocity components $(\tilde{u}, \tilde{v}, \tilde{w})$ associated with (x, η, z) are used to preserve the form of the transport terms, that is to have $u^*\partial_x + v^*\partial_y + w^*\partial_z = \tilde{u}\partial_x + \tilde{v}\partial_\eta + \tilde{w}\partial_z$. They are defined by $\tilde{w} = w^*$ and

$$\begin{pmatrix} \tilde{u} \\ T\tilde{v} \end{pmatrix} = \begin{pmatrix} 1 & 0 \\ -S & 1 \end{pmatrix} \begin{pmatrix} u^* \\ v^* \end{pmatrix}. \tag{4}$$

The continuity condition $(u^*_x + v^*_y + w^*_z = 0)$ becomes

$$\tilde{u}_x + \tilde{v}_\eta + \tilde{w}_z + \frac{S_\eta}{T}\tilde{u} + \frac{T_\eta}{T}\tilde{v} = 0. \tag{5a}$$

The x-momentum equation becomes

$$\tilde{u}_t + \tilde{u}\tilde{u}_x + \tilde{v}\tilde{u}_\eta + \tilde{w}\tilde{u}_z = -p_x + \frac{S}{T}p_\eta$$

$$+\nu\left(\tilde{u}_{xx} + \frac{1+S^2}{T^2}\tilde{u}_{\eta\eta} - \frac{2S}{T}\tilde{u}_{x\eta} + \left(-\frac{S_x}{T} + \frac{2SS_\eta}{T^2} - \frac{(1+S^2)T_\eta}{T^3}\right)\tilde{u}_\eta + \tilde{u}_{zz}\right), \tag{5b}$$

where p is the kinematic pressure. Similar terms appear for the other components. Now that all the derivatives have been taken, the normalization can be applied,

which will simplify the equations: η is identified to y and T is set to 1. The equations become

$$\tilde{u}_x + \tilde{v}_y + \tilde{w}_z + S_y \tilde{u} = 0, \tag{6a}$$

$$\tilde{u}_t + \tilde{u}\tilde{u}_x + \tilde{v}\tilde{u}_y + \tilde{w}\tilde{u}_z = -p_x + Sp_y + \nu(\tilde{u}_{xx} + (1+S^2)\,\tilde{u}_{yy} - 2S\tilde{u}_{xy} + (2SS_y - S_x)\,\tilde{u}_y + \tilde{u}_{zz}). \tag{6b}$$

Let us proceed with the Taylor expansion of the equations. The velocity and pressure are split into mean and fluctuating quantities: e.g. $\tilde{u} = U + u$, and the fast and slow derivatives defined by (2) are introduced. The friction velocity u_τ/U_∞ is a small quantity and tends to 0 (although slowly) as the Reynolds number tends to ∞. Let u_τ/U_∞ be of order ϵ. The velocity fluctuations u/U_∞, v/U_∞ and w/U_∞ are of the same order. The pressure fluctuations p/U_∞^2 are of order ϵ^2. The momentum equation ($\mathrm{d}\theta/\mathrm{d}x = u_\tau^2/U_\infty^2$) and the fact that θ is of the order of $\epsilon\delta$ show that the rate of change of δ in the x-direction is of order ϵ. S and $\delta A_X/A$ are of order ϵ. All of the slow derivatives like U_X and u_X are an order of magnitude smaller than the quantity itself, whereas the fast derivatives are of the same order as the quantity (taking δ as the lengthscale). For instance $u/U_\infty = O(\epsilon)$, $u_x\delta/U_\infty = O(\epsilon)$, $u_X\delta/U_\infty = O(\epsilon^2)$. The Taylor expansion of (6) up to order ϵ^2 is as follows

$$V_y + [U_X + S_y U] = 0, \tag{7a}$$

$$u_x + v_y + w_z + [u_X + S_y u] = 0, \tag{7b}$$

$$U_t + u_t + (U+u)\,u_x + v(U+u)_y + wu_z + [UU_X + VU_y + Uu_X + U_X u + Vu_y] = -p_x - [P_X] + \nu(U_{yy} + \nabla^2 u), \tag{7c}$$

$$v_t + (U+u)\,v_x + vv_y + wv_z + [Uv_X + (V_y + 2US_y)\,v + Vv_y] = -p_y + \nu\nabla^2 v, \tag{7d}$$

$$w_t + (U+u)\,w_x + vw_y + ww_z + [Uw_X + Vw_y] = -p_z + \nu\nabla^2 w. \tag{7e}$$

This is the set of equations that is integrated in time to obtain the turbulent fields. For each station of the boundary layer, a separate simulation is done using (7) with periodic conditions in x and z.

Note that the corrections in the viscous terms have been neglected. The mean and fluctuating components of the continuity equation are separated for clarity ((7*a*) and (7*b*)) and all three components of the momentum equation are shown. The U_t term in (7*c*) allows the flow to equilibrate, and vanishes once equilibrium has been reached. These equations are the Navier–Stokes equations, as usually written for a shear flow that is homogeneous in x and z, with the addition of 'growth terms' that are indicated by square brackets and can be interpreted as follows. The term $U_X + S_y U$ in the continuity equation (7*a*) is a consequence of the streamwise evolution of the mean-velocity profile. In the sink flow, it was identically zero (Spalart 1986*b*). In the flat-plate flow, it is zero in the wall layer and positive farther from the wall, so that V becomes negative: non-turbulent fluid is entrained into the boundary layer (in the new coordinates the dashed lines of figure 1(*a*) are parallel and the streamlines are directed towards the wall). The meaning of the $u_X + S_y u$ term in (7*b*) is not as clear (it was zero in the sink flow as well). Actually the numerical method used, which employs basis functions that satisfy $u_x + v_y + w_z = 0$ (causing the pressure term to be eliminated), does not allow the $u_X + S_y u$ term to be included. Thus the expansion is not fully second-order accurate in ϵ, but this effect is not thought to be very significant. In the momentum equation, the terms $UU_X + VU_y$ and P_X are mean momentum-transport and pressure terms. The term P_X is independent of y, to order

ϵ^3, and satisfies Bernoulli's equation in the freestream: for large y, $UU_X = -P_X$ (in the present application, $P_X = 0$). The terms $Uu_X + Vu_y$, $Uv_X + Vv_y$ and $Uw_X + Vw_y$ represent transport, or advection, of the turbulence by the mean flow. The term $2US_y v$ in (7*d*), which is due to the expansion of the coordinate lines, seems harder to interpret.

Finally, the terms $U_X u$ and $V_y v$ arise from the straining of the turbulence by the mean flow. However it would be misleading to imply that straining is accurately represented, because the numerical domain does not become deformed in time as in, for instance, Rogallo's homogeneous-turbulence simulations (1981). This weakness of the present approach is, ultimately, due to the fact that the approximation in (1) was based primarily on energy considerations, with little consideration of structural aspects. If one examines the influence of S (which is arbitrary to some extent), one finds that the mean growth term $UU_X + VU_y$ is not sensitive to S, because of the definition of the contravariant velocities $\tilde{u}$ and $\tilde{v}$ (if S changes, the quantities UU_X and VU_y change, but their sum remains equal to $U^*U^*_x + V^*U^*_y$). For the fluctuations the situation is more subtle. It can be shown that the global effect on a Reynolds stress such as $\langle u^2 \rangle$ behaves like the effect on the mean flow, that is, a change in S causes only a transfer between the terms $U \langle u^2 \rangle_X$ and $V \langle u^2 \rangle_y$. However, locally the value of S does matter because u_X and u_y do not have the same phase.

2.3. *Long-scale analysis*

The long-scale analysis provides the values of the quantities S, U_X, u_X, v_X and w_X that enter the growth terms in (7). In the method used for sink-flow boundary layers (Spalart 1986*b*) the long-scale analysis was simple; the flow was assumed to be self-similar both in terms of its lengthscales (all proportional to the distance X_0 from the sink) and its velocity scales (all proportional to the edge velocity Q/X_0). Thus one had the equations $S = -y/X_0$, $U_X = U/X_0$, $u_X = u/X_0$, etc.

In more general flows one has to consider two lengthscales in the y-direction: the wall length scale ν/u_τ and the boundary-layer thickness δ. There are also two velocity scales: the friction velocity u_τ and the edge velocity U_∞. Spalart & Leonard's (1985) study of boundary layers with pressure gradients was restricted to 'equilibrium' boundary layers in the sense used by Clauser (1954): they satisfied the defect law. The wall region was also assumed to obey the law of the wall. The coordinate η was (a function of) y^+ in the wall region and (a function of) y/δ in the outer region; a smooth blending between the two regions was made. The fluctuations were assumed to scale with u_τ both in the wall region (for constant y^+) and in the outer region (for constant y/δ). This assumption was consistent with the assumption made for the mean velocity and with the literature.

Spalart & Leonard's analysis has several shortcomings. It is limited to 'equilibrium' boundary layers, which are rare in practice. It was also shown by Coles (1962) that even in the simplest and best explored of equilibrium boundary layers, the constant-pressure flow, the defect law is not satisfied at low Reynolds numbers such as the one used for the simulations. Also, the overlap of a law of the wall and an outer-layer law requires a log layer in the mean velocity and a constant layer in the Reynolds stresses. The log layer was obtained by Spalart & Leonard, but the constant-stress layer was not. Although this could be a low-Reynolds-number effect, it is hard to explain why the log layer was well indicated at the same Reynolds number. Finally, simulations conducted at different Reynolds numbers yielded results in which the Reynolds stresses, near the wall, did not scale with u_τ and y^+. Instead they showed a consistent tendency to rise with the Reynolds number.

These various shortcomings indicated that (except for the sink flow) a valid study of boundary layers at low Reynolds numbers or with general pressure gradients should do away, at least, with the assumptions of a defect law and of the wall scaling of the Reynolds stresses. This led to the idea of obtaining the information needed to prescribe S, U_X, and so on, not from some assumptions but directly by conducting simulations at several stations of the same boundary layer. The X-derivatives are now obtained by taking differences between the different stations. This approach is more general and conceptually simpler. On the other hand it is more expensive, since several simulations have to be conducted. Also, the simulation of any one station requires upstream information. Thus one loses one of the advantages of the original procedure; however, the upstream information needed is reduced to mean-velocity and Reynolds-stress profiles. Time-dependent turbulent inflow values are not needed.

The first task is to define the coordinate lines to obtain S. The quantities y^+, near the wall, and y/δ, away from the wall, appear as 'natural' coordinates in the sense that they minimize the non-homogeneity along a constant-η line, thus making the growth terms as small as possible. The new coordinate η is defined explicitly as a weighted average of y^+ and y/δ:

$$\eta \equiv \frac{y_2^p(10^{-3}y^+)+y^p(y/\delta)}{y_2^p+y^p}, \tag{8}$$

where $y_1^+ \equiv 15$, $y_3/\delta \equiv 0.3$, $y_2 \equiv (y_1 y_3)^{\frac{1}{2}}$ and $p \equiv 5/\log_{10}(y_3/y_1)$. This rather arbitrary definition was chosen to ensure that η is a monotonic function of y, is equal to 10^{-3} y^+ for small y and to y/δ for large y, and makes a smooth transition between the two. Note that a nonlinear formula was needed because ν/u_τ and δ do not grow at the same rate in x.

Now that η is defined, if one knows the state of the flow at two values of X, e.g. X_1 and X_2, one computes an approximation to $S \equiv \partial y/\partial X$ by taking differences:

$$S \approx \frac{y(X_2,\eta)-y(X_1,\eta)}{X_2-X_1}. \tag{9}$$

Typically the flow at the upstream station, X_1, is known from a previous simulation and the flow at the downstream station, X_2, is being computed. Similarly U_X is approximated by $[U(X_2,\eta)-U(X_1,\eta)]/(X_2-X_1)$. For u, only the ratio A_X/A is needed and it is given by $[u_{\rm rms}(X_2,\eta)/u_{\rm rms}(X_1,\eta)-1]/(X_2-X_1)$ (recall that the role of A in (1) was to be proportional to the r.m.s. of the fluctuations). The formula for w is the same. Finally, the formula for v is slightly different: $A_X/A \approx [v_{\rm rms}(X_2,\eta)/v_{\rm rms}(X_1,\eta)-1]/(X_2-X_1)-S_y$. The $-S_y$ term is introduced by the normalization of $\tilde{v}$ in (4). This cancels half of the $2US_y v$ term of (7*d*). The only information one needs at X_1 is U, $u_{\rm rms}$, $v_{\rm rms}$ and $w_{\rm rms}$ as a function of y.

3. Results

3.1. *Choice of the parameters*

The periods in the x- and z-directions are $\Lambda_x = 100\delta^*$ and $\Lambda_z = 25\delta^*$. The spacing between collocation points, in wall units, is $\Delta x^+ \approx 20$, with $\Delta z^+ \approx 6.7$, and may vary by $\pm 5\%$ from one case to another. In the y-direction the number of points is adjusted so that there are 10 (non-uniformly spaced) points within 9 wall units of the wall. As a result of these requirements and of the need to factorize the length of the

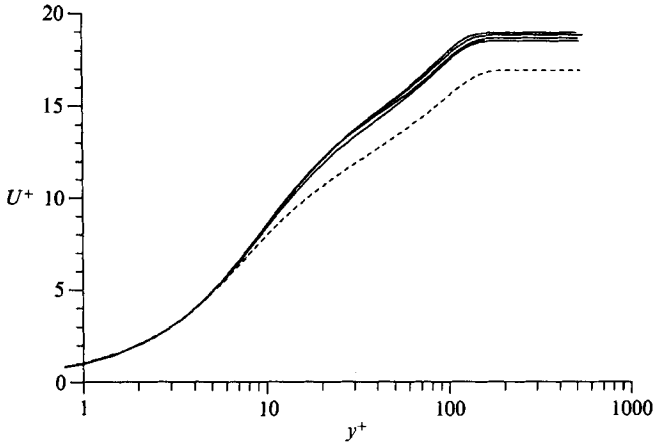

FIGURE 2. Resolution check at $R_{\delta*} = 500$. ---, coarse resolution; ——, all other cases.

fast Fourier transforms, the number of points in the x-, y- and z-directions is $(128 \times 50 \times 96)$ at $R_{\delta*} = 500$, $(256 \times 64 \times 192)$ at $R_{\delta*} = 1000$ and $(432 \times 80 \times 320)$ at $R_{\delta*} = 2000$. This last case has about 1.1×10^7 grid points, so 3.3×10^6 modes (using the $\frac{2}{3}$ rule in each direction, Spalart 1986*a*). The timestep is adjusted so that the maximum local CFL number (see Spalart 1986*a* for the exact definition) is 2. As a result the non-dimensional timestep $\Delta t U_\infty/\delta^*$ is about 0.3, 0.14 and 0.07 at $R_{\delta*} = 500$, 1000 and 2000 respectively. In wall units, the non-dimensional timestep $\Delta t u_\tau^2/\nu$ is about 0.43, 0.32 and 0.29 respectively. The time sample for the statistics is of the order of $200\delta^*/U_\infty$ (larger samples would help improve the smoothness of the spectra, but would be very expensive to generate). The sample can be compared with a typical timescale of the turbulence, the ratio of its energy to its production rate. Near the wall this timescale is about 15 wall time units, so about $3\delta^*/U_\infty$ (at $R_{\delta*} = 1000$). In that sense, in a time of $200\delta^*/U_\infty$ the turbulent energy is dissipated and regenerated 67 times. There is little doubt that the turbulence has reached a statistically steady state, and could be maintained indefinitely.

These parameter values were chosen by monitoring the spectra, both at their lower end (to choose the period) and at their upper end (to choose the grid spacing). Alternatively, the two-point correlations can be used (Spalart 1986*a*). Two tests were also performed for the (relatively inexpensive) case $R_{\delta*} = 500$ to further validate the choice of the parameters. In the first test, the values of Λ_x and Λ_z were doubled, then halved, and the grid spacing left unchanged (thus the number of points in x and z also changed by a factor of 2). In the second test, the simulation was rerun with both much finer, and then much coarser resolution (the number of points in x and z was doubled, then halved; the number of points in y was varied from its basic value of 50 to 64, then 40). The timestep, being regulated by the value of the CFL number, is also reduced when finer resolution is used so that both the spatial and temporal errors are reduced.

Figure 2 displays the sensitivity of the mean-velocity profile to the numerical parameters. The difference between the basic simulation and the 'improved' ones (larger periods or finer resolution) is small. This figure allows one to estimate the remaining numerical uncertainty. The simulation with reduced periods gives results very close to the basic simulation, which indicates that the periods that were chosen to obtain satisfactory long-range behaviour (low correlations at a distance $\frac{1}{2}\Lambda$) are

more than sufficient to obtain a satisfactory velocity profile. On the other hand, the simulation with coarse resolution gives significantly different results, including a much higher value of u_τ/U_∞. Thus the resolution chosen appears to be adequate, but not wasteful. The sensitivity of other statistical quantities up to third-order moments was found to be small. For fourth-order moments, the u- and w-components showed a moderate sensitivity, but the flatness factor of v was very sensitive near the wall: it varied from about 4 with coarse resolution to over 30 with fine resolution. Away from the wall, the profiles agreed well again, even the v-flatness. Thus one should consider statistics for moments beyond third order with some caution, at least near the wall.

3.2. *Streamwise evolution of the mean flow*

Four stations of the boundary layer were simulated, with $R_{\delta^*} = 400$, 500, 1000 and 2000 respectively. The values of R_θ are approximately 225, 300, 670 and 1410. Detailed results from the first station, $R_{\delta^*} = 400$, will not be shown. It was computed using the approach of Spalart & Leonard (1985). While this approach was shown to have some deficiencies, it is satisfactory for the generation of upstream data.

The possibility of obtaining turbulence at $R_\theta = 225$ is in disagreement with Preston's (1957) often-quoted estimate that the lowest Reynolds number at which 'fully developed turbulent flow' can occur is 320. It is based on a comparison between pipe-flow and boundary-layer data, and on the rather abstract argument that when the length of the log layer is reduced to zero (because the inner and outer regions overlap), fully developed turbulence cannot exist. One may need to distinguish between the concepts of 'fully developed' turbulence and of 'sustained' turbulence. Indeed, in the present results for R_θ below about 600, a normal log layer is not observed (see below). However, the turbulence was sustained. Bandyopadhyay (1987) was able to generate a turbulent boundary layer at $R_\theta = 285$. A comparison with sink-flow boundary layers may also be useful. When these flows were studied with the present method (Spalart 1986*b*) the threshold Reynolds number was found to be $R_\theta = 330$, which is in good agreement with experimental data. In sink-flow simulations, the turbulence quickly collapsed when the Reynolds number was lowered to below 330; thus the method seems reliable. The sink flow has a strong favourable pressure gradient, which has a stabilizing effect (it is known to inhibit transition and to induce relaminarization). When this stabilizing effect is removed, turbulence should be sustained at lower Reynolds numbers. Curiously, Preston's argument about the overlap of the inner and outer region predicts the opposite effect: the limit would be lower with a favourable pressure gradient. Thus Preston's estimate for the sink flow would be significantly lower than the value 330, which has now been obtained by two independent approaches.

Figure 3 shows the growth of the displacement- and momentum thicknesses in the streamwise direction. Since the origin is arbitrary in the x-direction, the notation ΔR_x is used to represent the Reynolds number based on the distance from the first station and on U_∞. The scale is enlarged in the normal direction. The momentum-balance equation, $\mathrm{d}(R_\theta)/\mathrm{d}(R_x) = \frac{1}{2}c_\mathrm{f}$, is checked by drawing segments centred on the R_θ points with a slope of $\frac{1}{2}c_\mathrm{f}$. They show that the balance equation is satisfied (with the derivative at X_2 approximated as in (9)) and that the spacing between stations is small enough. In figure 4 the dependence of the friction coefficient c_f and the shape factor $H \equiv \delta^*/\theta$ on R_θ is shown; it compares well with experimental data (Coles 1962; Purtell *et al.* 1981; Murlis *et al.* 1982; Erm *et al.* 1985). However, as R_θ increases, the c_f decreases slightly less than the experiments show. Figure 2 suggests that the

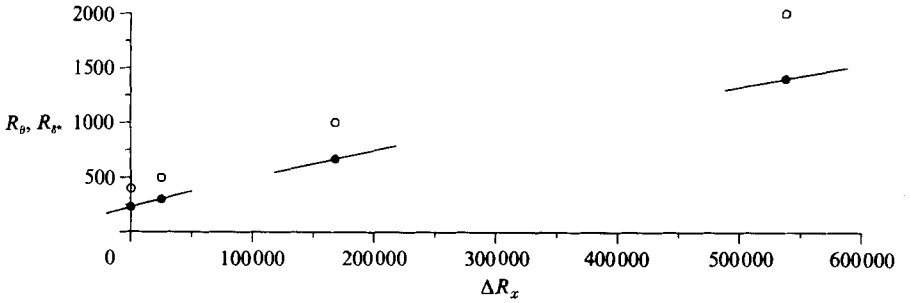

FIGURE 3. Streamwise thickening of the boundary layer. ○, displacement thickness δ^*; ●, momentum thickness θ; —●—, slope $\frac{1}{2}c_f$.

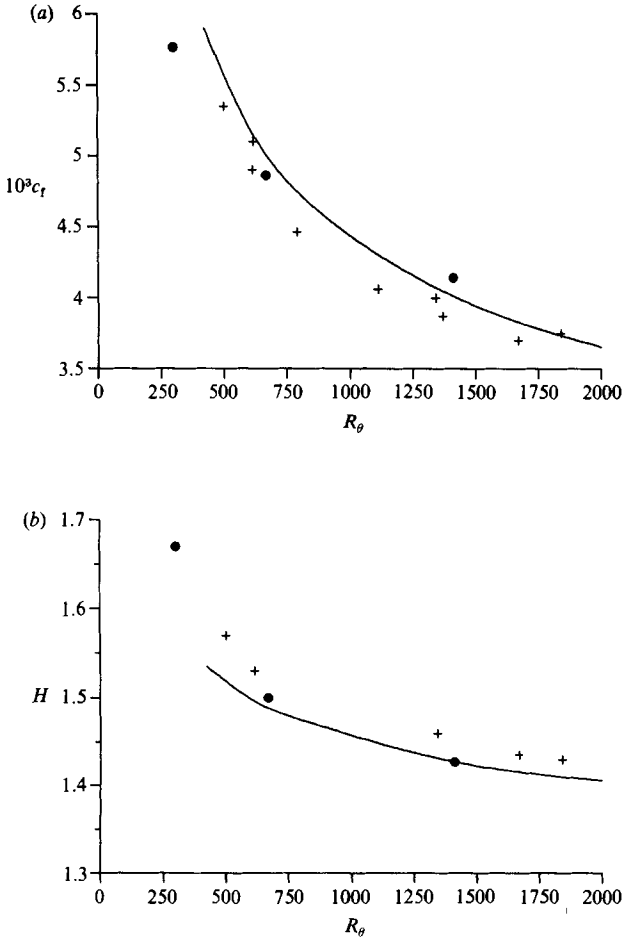

FIGURE 4. Streamwise evolution of the boundary layer, ●, present results; ——, Coles; +, other experiments. (*a*) Friction coefficient c_f; (*b*) shape factor H.

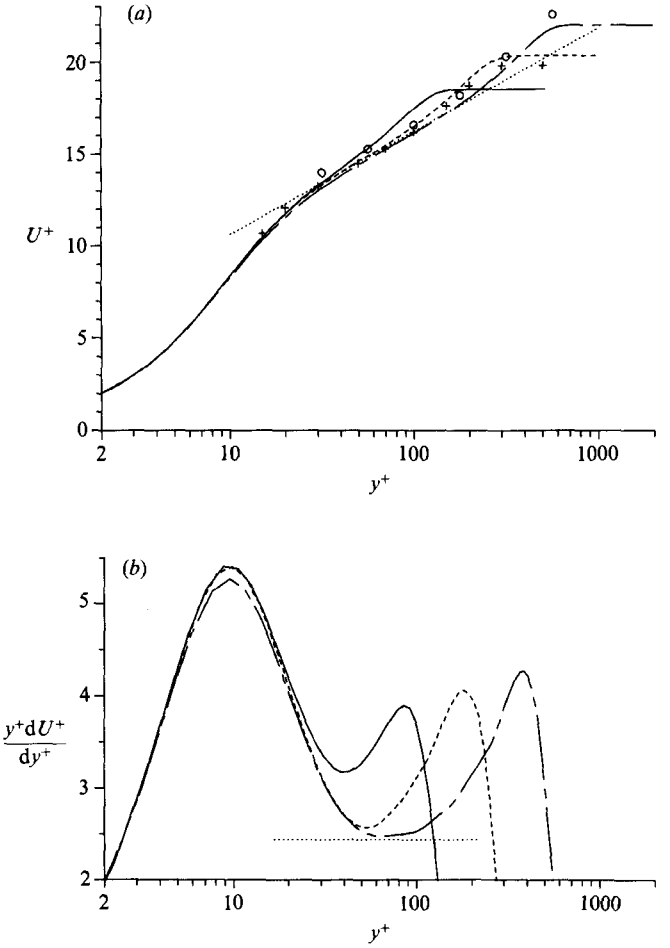

FIGURE 5. Mean-velocity profile and its derivative. ——, $R_\theta = 300$; – – –, $R_\theta = 670$; — — —, $R_\theta = 1410$; ···, log law $U^+ = \log(y^+)/0.41 + 5$; +, $R_\theta = 617$ (Erm *et al.* 1985); ○, $R_\theta = 1368$ (Murlis *et al.* 1982). (*a*) U^+; (*b*) $y^+ dU^+/dy^+$.

uncertainty on U_∞/u_τ is of the order of ± 0.25. This translates into ± 0.12 for $10^3 c_f$, which is of the same order as the differences in figure 4(*a*) (for $R_\theta = 670$ and up). The $R_\theta = 1410$ simulation was continued with slightly improved resolution (96 points in y instead of 80); the c_f showed no tendency to decrease. The error could also be caused by effects neglected in the multiple-scale approximation; unfortunately it does not seem possible to estimate these effects quantitatively.

The mean velocity profiles are plotted in figure 5(*a*) using wall variables. All the averages are taken in x, z and t. Experimental results at $R_\theta = 617$ (Erm *et al.* 1985) and 1368 (Murlis *et al.* 1982) are also plotted and may be compared with the present results at $R_\theta = 670$ and 1410. For R_θ equal to 670 and larger, the profiles closely follow the logarithmic law $U^+ = \log(y^+)/\kappa + C$, with constants $\kappa = 0.41$ and $C = 5$, starting at $y^+ \approx 30$. For $R_\theta = 300$, the curve is significantly higher in that region; however it is still rather straight. This raises the question of exactly how the log layer is defined.

A logarithmic layer is a region in which the quantity $dU/d(\log y)$, or $y\,dU/dy$, is constant and equal to u_τ/κ. In high-Reynolds-number boundary layers, this region

is long and bounded on both sides by regions in which $y\,\mathrm{d}U/\mathrm{d}y$ takes values larger than the constant. Thus the logarithmic layer and the value of u_τ/κ can be found by seeking the minimum of $y\,\mathrm{d}U/\mathrm{d}y$ *vs.* y (this amounts to seeking the inflexion point in figure 5*a*). The value of C can then be determined at the same position. This seems to be the only rigorous definition. The usual procedure of adjusting κ and C until the straight line fits the velocity profile 'well' in the coordinates of figure 5(*a*) is not exempt from arbitrariness. Of course, the procedure based on $y\,\mathrm{d}U/\mathrm{d}y$ is more sensitive to noise, and will yield an erroneously low value of u_τ/κ for noisy data (C may then be overpredicted). Thus it may not be applicable to experimental data. However, in numerical results, the profiles of $y^+\,\mathrm{d}U^+/\mathrm{d}y^+$ show a low level of noise once the sample is sufficient, as shown in figure 5(*b*). Note that if the value of κ is assumed to be known, one can deduce the value of u_τ (and hence the wall stress) using only measurements in the log layer. This is essentially the method of the 'Clauser plot' (Clauser 1954).

When the Reynolds number is low, $y\,\mathrm{d}U/\mathrm{d}y$ still exhibits a local minimum, but a narrow one (figure 5*b*). Two interpretations are possible. The first is an 'infinitely short' log layer. Figure 5(*b*) shows that at $R_\theta = 300$, this log layer has a low value of about 0.315 for the 'apparent Kármán constant' κ'. This is reminiscent of Simpson's interpretation (1970), although Simpson made deductions from measurements taken in the outer region of the flow. He proposed the law $\kappa' = \kappa_0(R_\theta/6000)^{\frac{1}{8}}$ with κ_0 the asymptotic value, about 0.40. This yields 0.28, 0.31 and 0.34 for our three cases. The present results indicate values of 0.32, 0.38 and 0.40 for κ'. They show a smaller departure of κ' from κ_0, and the value of κ' is essentially unaffected down to $R_\theta \approx 670$. The apparent values C', in the numerical results, are 2.5, 4.3 and 4.7 for the three cases. The uncertainty is estimated to be about ± 0.01 for κ' and ± 0.25 for C'.

The second and preferred interpretation is simply that the log layer exists at $R_\theta = 670$ but has disappeared at $R_\theta = 300$. The log layer normally covers the region between $y^+ \approx 30$ and $y/\delta \approx 0.15$. The wall and wake regions begin to overlap for R_θ lower than 400, so that the local minimum of $y^+\,\mathrm{d}U^+/\mathrm{d}y^+$ is reduced to a point and is higher than its normal value. The results in figure 5 imply that at $R_\theta = 300$, the Clauser-plot method yields an erroneously high 'apparent friction velocity' u'_τ if the decrease in κ' is ignored (u'_τ equals $u_\tau \kappa_0/\kappa'$ in which u_τ is the true friction velocity). Curiously, at $R_\theta = 300$ the 'apparent log layer' obtained by fitting a straight line through the inflexion point of the profile (at $y^+ \approx 40$) follows the velocity profile closely up to a high value of y/δ: about 0.35 as opposed to 0.15 normally. Purtell *et al.* (1981) also remarked on the tendency of the log layer to extend to larger values of y/δ at low Reynolds numbers.

The 'strength of the wake' ΔU^+ is defined by Coles (1962) as the maximum value of $(U^+ - U^+_{\log})$, the deviation of the velocity profile over the log law (which occurs in the region near $y/\delta = 0.8$). The quantity is constant, with a value of about 3, at high Reynolds numbers when the defect law is satisfied, but decreases for values of R_θ lower than about 6000 (Coles 1962). This is a prime example of low-Reynolds-number effect. In defining ΔU^+ at low Reynolds number, one has to choose between the 'apparent' log layer and the normal log layer ($\kappa = 0.41$, $C = 5$). Furthermore, the value of ΔU^+ is very sensitive to the constants used for the log layer. If C is changed from 5.0 (Coles 1962) to 5.2 (Murlis *et al.* 1982) ΔU^+ is clearly reduced by 0.2; if κ is changed from 0.40 to 0.41 ΔU^+ is increased by about 0.4 (at $R_\theta = 1410$) which is about 25%. Figure 6 compares the computed values of ΔU^+, using both definitions, with Coles' curve and other experimental results by Murlis *et al.* (1982) and Erm *et al.* (1985). The curve based on the apparent log law rises like the experimental curves,

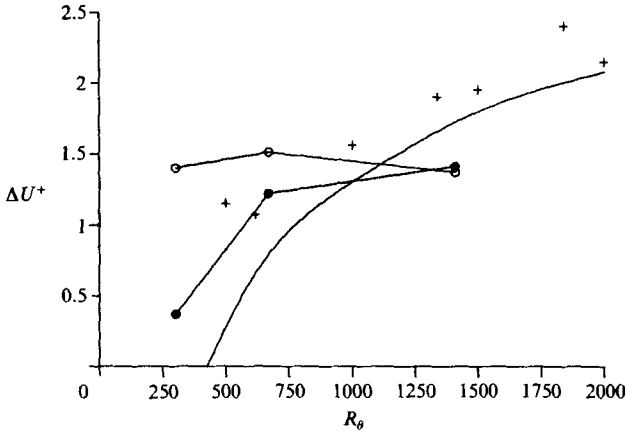

FIGURE 6. Strength of the wake, ΔU^+. Present results: —●—, based on apparent log law; —○—, based on normal log law. ——, Coles; +, other experiments.

but the trend in the other curve (based on $\kappa = 0.41$, $C = 5.0$) is very different: it is essentially flat with values of about 1.4, much lower than the accepted value of 3. This trend was already apparent in figure 5(*a*). Very accurate measurements or simulations over a wide Reynolds-number range, as well as a strong consensus on the value of κ (at least two significant digits), will be needed before definitive results are obtained for ΔU^+.

A reliable definition of the boundary-layer thickness δ is needed to express the results in the upper part of the flow. The definition of δ as the point where U/U_∞ takes a given value (typically 0.99 or 0.995) is not very satisfactory. It depends on small differences; it is inconsistent with the defect law since u_τ depends on x. The situation is especially confusing at low Reynolds numbers since the velocity profile is not invariant, whether it is normalized by U_∞ or u_τ. On the other hand, the shear-stress profile is very close to invariant when normalized by its wall value as will be shown. Let $\tau(y)$ be the total stress and $\tau(y)^+$ denote $\tau(y)/\tau(0)$; τ^+ varies smoothly from 1 to 0 as y varies from 0 to ∞. Let the 'stress thicknesses' δ_1 and δ_2 be defined by

$$\delta_1 \equiv \int_0^\infty \tau^+(y)\,\mathrm{d}y, \quad \delta_2 \equiv \int_0^\infty \tau^+(y)\,(1-\tau^+(y))\,\mathrm{d}y.$$

These definitions were made by analogy with the definition of the velocity thicknesses δ^* and θ. One can define a 'stress shape factor' $H_\tau \equiv \delta_1/\delta_2$. For reference, the shape factors of a triangular and a rectangular stress distribution are 3 and $+\infty$, respectively. The Gaussian $\exp(-y^2)$ and the cubic $(1-3y^2+2y^3)$, although both bell-shaped, give quite different values: 3.41 and 3.88. Thus H_τ is a rather sensitive measure of the shape of the stress distribution. The values of H_τ at the four stations of the boundary layer are about 4.0, 3.9, 4.0 and 3.9; they are close to each other, and to the cubic. In contrast the velocity shape factors, H and Clauser's shape factor $G \equiv (U_\infty/u_\tau)(H-1)/H$ (which was designed to be invariant), are much more sensitive to low-Reynolds-number effects. See figure 4(*b*) for the values of H; G varies from 7.4 to 6.5. This suggests using the stress, instead of the velocity, to define the thickness δ. In order to relate this concept to the familiar concept of δ as the edge of the turbulent region, or of the region with mean shear, the following definition was adopted:

$$\delta \equiv 1.85\delta_1. \tag{10}$$

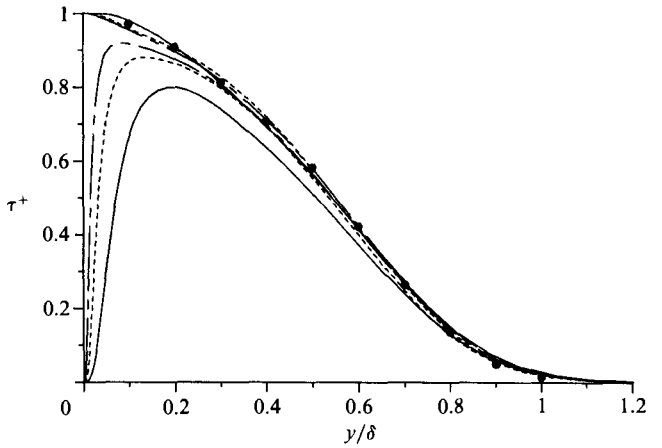

FIGURE 7. Shear-stress distribution. ——, $R_\theta = 300$; – – –, $R_\theta = 670$; —·—, $R_\theta = 1410$. Upper curve, total stress; lower curve, Reynolds stress. ●, $R_\theta \approx 7500$ (Klebanoff 1954).

The factor 1.85 gives a good match with published values, for instance Klebanoff's (1954). This definition has the advantage of being an integral instead of a local quantity; on the other hand, it applies only to the zero-pressure-gradient boundary layer. Figure 7 shows the shear-stress profiles plotted versus y/δ. The agreement with Klebanoff and the collapse of the total-stress profiles are very good, thus confirming the behaviour of H_τ and justifying the definition of δ. At $y = \delta$ the velocity U/U_∞ is equal to 0.9965, 0.9974 and 0.9977 for $R_\theta = 300$, 670 and 1410 respectively. The corresponding values of the defect $(U_\infty - U)/u_\tau$ are 0.065, 0.052 and 0.050. Finally, the values of τ^+ at $y = \delta$ are 0.028, 0.026 and 0.023. Definitions of δ based on any of these three 'reasonable' candidates were tried and produced values that differ from (10) by up to 5% and significantly degrade the collapse of the curves in figure 7, especially between 0.5δ and 0.8δ.

In figure 7 the total-stress profiles have zero slope at the wall, as they should since the flow is steady and the pressure gradient is zero, and one would naturally expect a parabolic behaviour for τ^+ near the wall. However, the profiles, at least for $R_\theta = 670$ and 1410, show a flat part around 0.1δ with finite slope, $\partial\tau^+/\partial(y/\delta)$ of about -0.5. A simple argument is outlined in the Appendix, which agrees with Townsend's 1956 analysis and was also mentioned recently by Li, Henbest & Perry (1986). It suggests that this behaviour is indeed correct, and that at high Reynolds numbers the total-stress profile approaches the wall with a finite slope of the order of -0.6, with the slope falling to zero only within the buffer layer (which becomes very thin compared with δ). This finding is significant, because it means that even the zero-pressure-gradient boundary layer does not contain a constant-stress layer. The stress behaves in a manner similar to a favourable-pressure-gradient flow, and the value -0.6 is of the same order as the value in a channel flow, namely -1 (defining δ as the channel half-width). Again, as in the sink flow, constant-stress behaviour cannot be invoked to justify the existence of the logarithmic layer (Spalart 1986*b*).

Figure 8 shows the velocity profiles, now plotted versus y/δ. In figure 8(*a*) the velocity U itself is plotted and normalized by U_∞. Again, experimental results at $R_\theta = 617$ and 1368 are plotted, and the agreement is quite good (for Erm *et al.*'s flow the following values were assumed: $u_\tau/U_\infty = 0.0505$, $\delta^+ = 324$; for Murlis *et al.*: $u_\tau/U_\infty = 0.0442$, $\delta^+ = 547$). In figure 8(*b*) the velocity defect $(U - U_\infty)/u_\tau$ is plotted; in

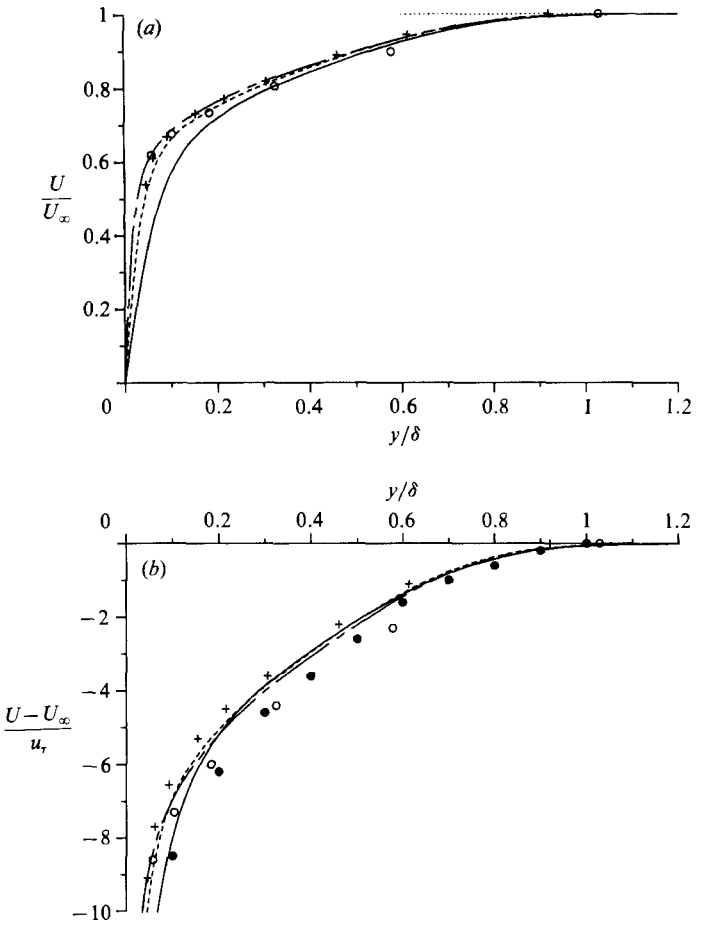

FIGURE 8. Mean-velocity profile. ——, $R_\theta = 300$; – – –, $R_\theta = 670$; – – –, $R_\theta = 1410$. +, $R_\theta = 617$ (Erm *et al.* 1985); ○, $R_\theta = 1368$ (Murlis *et al.* 1982); ●. $R_\theta \approx 7500$ (Klebanoff 1954). (*a*) U/U_∞; (*b*) $(U-U_\infty)/u_\tau$.

addition to Erm *et al.*'s and Murlis *et al.*'s results, the experimental results of Klebanoff (1954) at high Reynolds numbers are shown (assuming $u_\tau/U_\infty = 0.0375$). Again the agreement is acceptable but there is essentially no trend towards Klebanoff's high-Reynolds-number curve, as Coles' theory would predict. The numerical results seem to satisfy a defect law, but one that does not quite agree with Klebanoff's. Note that the results as presented in figure 8 depend on δ, which is not firmly defined. Note also that using the apparent friction velocity u'_τ (deduced from a Clauser plot) instead of the true u_τ to normalize $(U-U_\infty)$ in figure 8(*b*) would create a trend towards Klebanoff's curve and thus improve the agreement with Coles' model.

3.3. *Streamwise evolution of the turbulence*

The behaviour of the Reynolds shear stress $-\langle uv \rangle$ is predictable. As shown in figure 7 the normalized total stress τ^+, plotted versus y/δ, varies very little with the Reynolds number. In the same figure, the Reynolds shear stress $-\langle uv \rangle^+$ shows a weak sensitivity to the Reynolds number for y^+ larger than about 50. Near the wall, of course, the Reynolds stress falls to 0 at a different value of y/δ depending on the

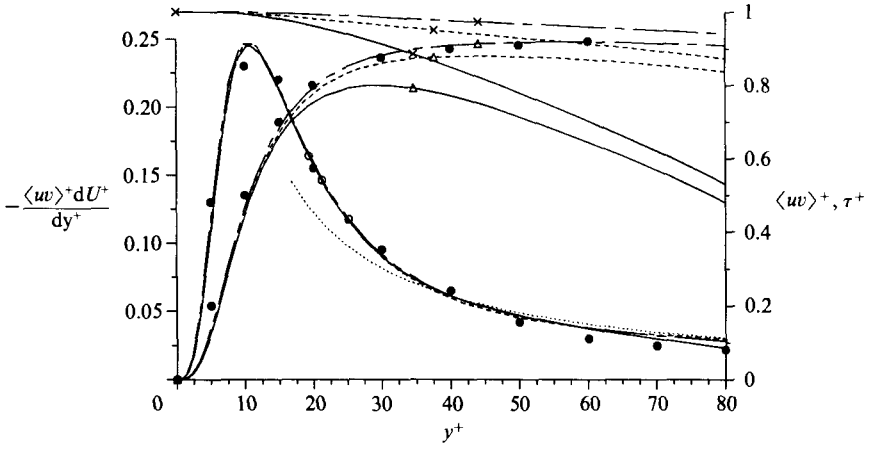

FIGURE 9. Stresses and production near the wall. ——, $R_\theta = 300$; – – –, $R_\theta = 670$; – — –, $R_\theta = 1410$ ···, $1/\kappa y^+$. △, Reynolds stress; ×, total stress; ○, production. ●, Kim *et al.* 1968.

sublayer thickness. Figure 9 shows both stresses and the turbulent-energy production $-\langle uv\rangle^+ dU^+/dy^+$ in the wall region. The stresses are rather insensitive to Reynolds number up to a y^+ of about 15, where the low-Reynolds-number profiles bend down. The outer region, in which the stress falls to zero, impinges on the inner region, in which the total stress is essentially constant. The higher-Reynolds-number Reynolds-stress profile agrees very well with Kim, Kline & Reynolds' (1968) experimental curve. The collapse of the production profiles is striking. They agree with each other, with Kim *et al.*'s curve, and with the theoretical profile $1/\kappa y^+$ even in the region where the Reynolds stresses are far from collapsing. At low Reynolds numbers the decrease of $-\langle uv\rangle^+$ and the increase of dU^+/dy^+ (figure 5) cancel each other in the product to a remarkable degree. This fact cannot be explained by traditional arguments.

The behaviour of the normal Reynolds stresses $\langle u^2\rangle$, $\langle v^2\rangle$ and $\langle w^2\rangle$ is more complex than that of the shear stress. The r.m.s. values of these fluctuations are plotted in figure 10 *vs.* y/δ, non-dimensionalized by u_τ, and compared with Klebanoff's (1954) results. The computed curves agree with Klebanoff's curves reasonably well except in the wall region, below $y^+ = 50$, where the Reynolds-number difference is felt. Outside this region the curves, at least for v and w, show a moderate but consistent rise with Reynolds number. Perry, Lim & Henbest (1985, see also Perry, Henbest & Chong 1986) explain this rise by the lengthening of the inertial range towards higher wavenumbers, the low-wavenumber part of the spectra being independent of Reynolds number. This hypothesis is supported by figure 11. Power spectra of the three velocity components are shown at $y = \frac{1}{2}\delta$, non-dimensionalized by u_τ and δ, for the $R_\theta = 300$ and 1410 cases. Spanwise spectra are shown, as they tend to be smoother than the streamwise spectra. Although the sample is marginal for the lowest wavenumbers, the indication is that with a larger sample the spectra will coincide well up to a $k_z\delta$ of about 10.

The theory implies that by extending the inertial range to infinite wavenumbers one should obtain the 'infinite Reynolds number' value for each Reynolds stress at each value of y/δ. Such an extension would add to the stress a correction $C_1'(u_k/u_\tau)^2$ in which C_1' is a universal constant, u_k is the Kolmogorov velocity $(\nu\epsilon)^{\frac{1}{4}}$, and ϵ is the dissipation rate. A value of 2.8 was assumed for C_1', which is smaller than Perry's

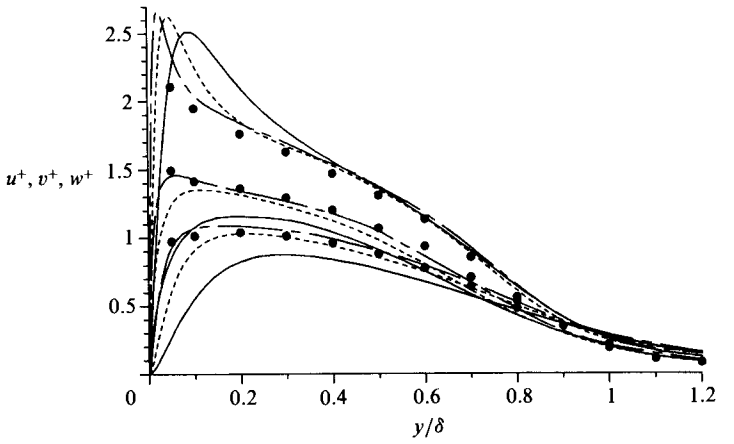

FIGURE 10. Turbulence intensities. Upper curve, $u_{\rm rms}/u_\tau$; lower curve, $v_{\rm rms}/u_\tau$; middle curve, $w_{\rm rms}/u_\tau$. ——, $R_\theta = 300$; – – –, $R_\theta = 670$; ——, $R_\theta = 1410$. ●, $R_\theta \approx 7500$ (Klebanoff 1954).

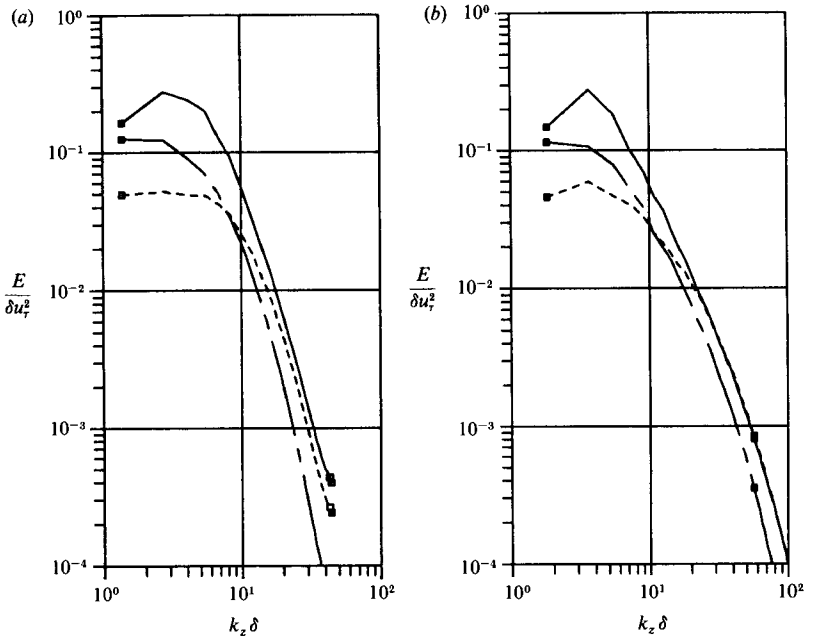

FIGURE 11. Spectra at $y = \frac{1}{2}\delta$. ——, $\langle u^2\rangle$; – – –, $\langle v^2\rangle$; ——, $\langle w^2\rangle$. (*a*) $R_\theta = 300$; (*b*) $R_\theta = 1410$.

value. This will be discussed later with the spectra (§3.4). For the computed flows the dissipation rates were available, whereas for Klebanoff's results the dissipation was estimated by scaling the dissipation computed in the $R_\theta = 1410$ simulation. Figure 12 shows that the correction dramatically improves the collapse of the profiles, except for $\langle u^2\rangle$ at $R_\theta = 300$ and near the boundary-layer edge ($y/\delta > 0.8$). In that region the turbulence is intermittent; the irrotational fluctuations, which do not follow Kolmogorov's theory, contribute a significant part of the energy. The agreement with Klebanoff's corrected values is also rather good. The profiles still do not collapse near the wall, for y^+ less than about 50, which could be expected since

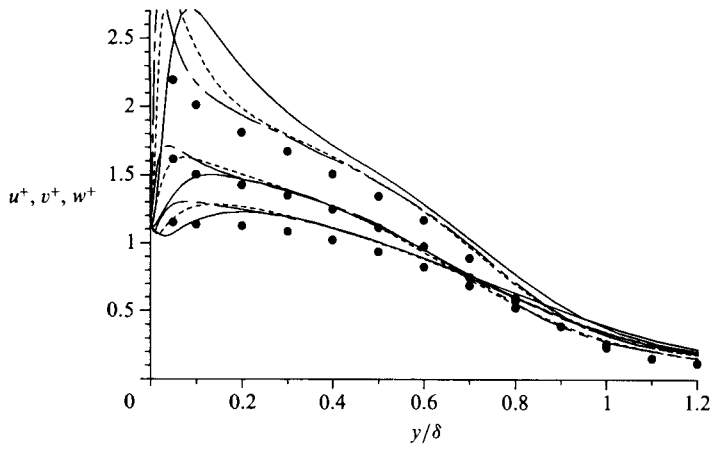

FIGURE 12. Turbulence intensities, corrected to infinite Reynolds number. Upper curve, $u_{\rm rms}/u_\tau$; lower curve, $v_{\rm rms}/u_\tau$; middle curve, $w_{\rm rms}/u_\tau$. ——, $R_\theta = 300$; – – –, $R_\theta = 670$; – – – –, $R_\theta = 1410$. ●, $R_\theta \approx 7500$ (Klebanoff 1954).

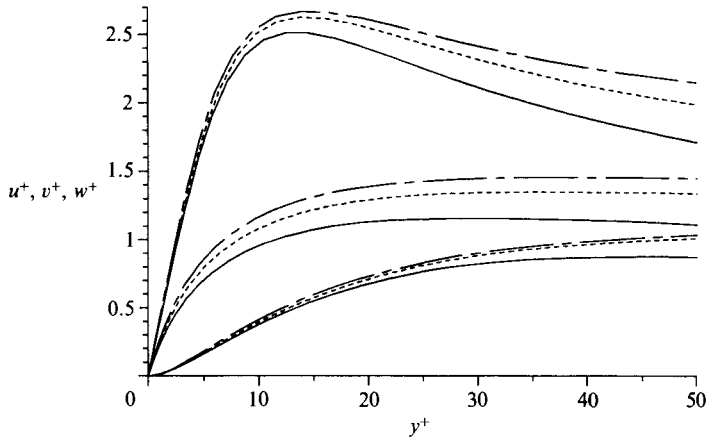

FIGURE 13. Turbulence intensities. Upper curve, $u_{\rm rms}/u_\tau$; lower curve, $v_{\rm rms}/u_\tau$; middle curve, $w_{\rm rms}/u_\tau$. ——, $R_\theta = 300$; – – –, $R_\theta = 670$; – – – –, $R_\theta = 1410$.

no inertial range exists in that region. The obvious similarities between the deviations observed near the wall suggest a model of the type $f_1(y/\delta)+f_2(y^+)$ where f_2 is zero for y^+ larger than about 50 (one could also try a product, $f_1(y/\delta)\times f_2(y^+)$); however, there is little theoretical support for such models.

The results in figure 12 confirm the validity of the scaling based on δ and u_τ, and of Perry *et al.*'s viscous correction (although with different constants). The possibility of extrapolating moderate-Reynolds-number simulation results to higher Reynolds numbers using just a simple argument and one universal constant C_1' is very attractive.

When shown in wall variables the profiles also rise with Reynolds number (figure 13). The behaviour of w is the most striking: the rise is significant even very near the wall. Experimentally, Coles (1978) and Purtell *et al.* (1981) observed that the r.m.s. of u increased with Reynolds number for y^+ larger than 15. Coles also reports a wide scatter in the w-values, but without a clear trend versus Reynolds number (1978, and

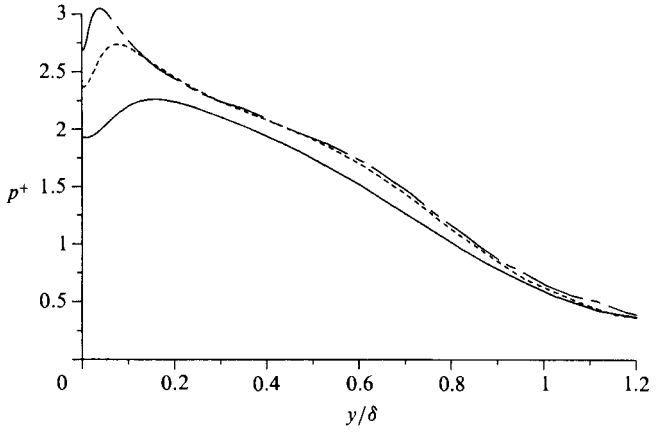

FIGURE 14. Pressure fluctuations. ——, $R_\theta = 300$; – – –, $R_\theta = 670$; – – – –, $R_\theta = 1410$.

personal communication 1985). The results in figure 13 are in sharp disagreement with the concept of wall scaling (based on u_τ and ν), a concept that was very successful when applied to the mean velocity. By directly extending the arguments from the mean velocity to the stresses one would predict a good collapse of all curves in figure 13 in the log layer and, *a fortiori*, near the wall. Note also that the viscous correction by $C_1'(u_k/u_\tau)^2$ could not improve the collapse in figure 13 because, at a given y^+, u_k/u_τ varies very little with Reynolds number.

Figure 14 shows the r.m.s. of the pressure fluctuations, normalized by u_τ^2. The behaviour is very similar to the velocity r.m.s.: a slight rise with Reynolds number in the outer region but a strong rise near the wall. The wall value rises from about 1.9 to 2.7. The agreement with Schewe's (1983) careful measurements at $R_\theta = 1400$ is excellent; he obtained about 2.66. The trend is in agreement with experimental results reviewed by Willmarth (1975), and is consistent with Townsend's (1976) law for the wall value, $\langle p^2 \rangle / u_\tau^4 = C' \log(\delta^+) + D$ with for C' a value of about 2.

The vorticity intensities collapse well when plotted versus y/δ and normalized with the 'mixed' scale $(u_\tau^3/\delta\nu)^{\frac{1}{2}}$ (which is appropriate for the dissipative motion), but again show a significant rise with Reynolds number when plotted in wall units. This lack of collapse of the velocity, pressure and vorticity intensities near the wall has important implications for theories and turbulence models. Apparently, one cannot rely on a 'law of the wall' for these quantities as for the mean velocity and the shear stress. Note that the multiple-scale approximation that was made is probably most valid near the wall, where the natural length- and timescales are the smallest. The growth terms are also very small near the wall. Thus, it is unlikely that the surprising behaviour of the turbulence statistics near the wall could be due to the approximations that were made.

The Reynolds-number effects in figures 13 and 14 can be interpreted in terms of the theory of 'active' and 'inactive' motions proposed by Townsend (1961) and Bradshaw (1967). This theory was initially developed to explain the observation that some of the triple correlations were Reynolds-number dependent near the wall. The active motion 'produces the shear stress and its statistical properties are universal functions of τ and y'; the inactive motion is 'effectively irrotational' and does not produce shear stress (Bradshaw 1967). The inactive motion has length- and timescales that are large compared with the viscous-layer scales, and is not directly

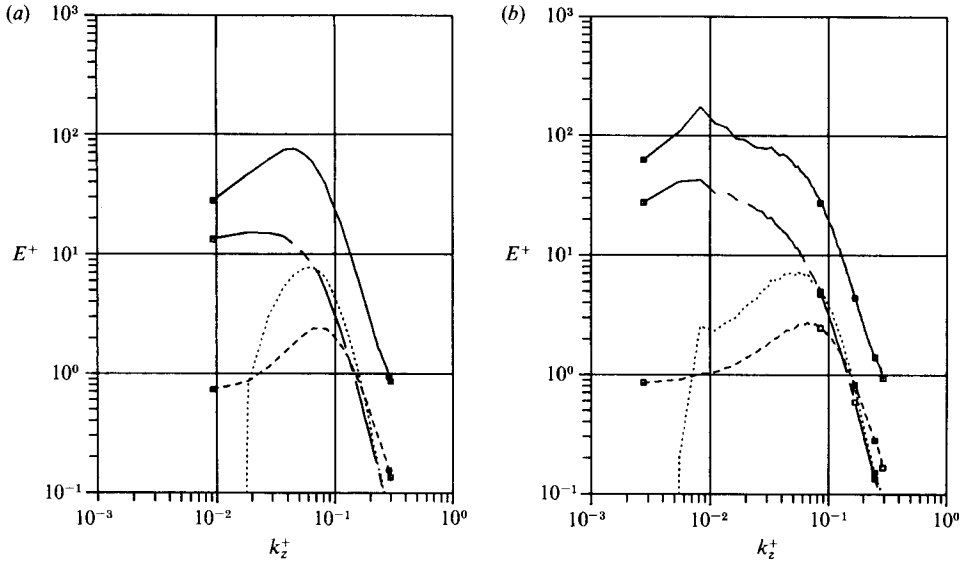

FIGURE 15. Spectra at $y^+ = 15$. ——, $\langle u^2 \rangle$; – – –, $\langle v^2 \rangle$; ——, $\langle w^2 \rangle$; ···, $-\langle uv \rangle$. (*a*) $R_\theta = 300$; (*b*) $R_\theta = 1410$.

connected with the wall shear stress. Therefore it may not scale with u_τ and ν (Townsend 1976, p. 138).

Figure 15 identifies the lengthscales responsible for the extra energy at higher Reynolds numbers. The power spectra of the four non-zero components of the Reynolds-stress tensor are shown. The wavenumber and the energy are non-dimensionalized using wall variables (u_τ and ν). Spanwise spectra are presented, in the $y^+ = 15$ plane, for the cases $R_\theta = 300$ and 1410. Figure 15 shows that as the Reynolds number increases, the energy of fluctuations with wavelengths less than about 150 wall units is not affected. In the x-direction, only waves longer than about 300 wall units show deviations. Thus, wall scaling is violated only by those scales of motion much larger than the thickness of the wall layer (roughly 50 wall units). These large-scale motions contribute most to $\langle w^2 \rangle$ and little to $\langle v^2 \rangle$ and $-\langle uv \rangle$. This agrees well with the concept of inactive motion.

A simple model of the inactive motion is that the pressure disturbance following a large coherent structure, combined with the no-slip condition, create a situation similar to Stokes' oscillating boundary layer (Schlichting 1979). From the known solution to this equation one can predict the dependence of the energy on y^+. If one takes a typical wavenumber $k_x^+ \approx 0.005$, for which the spectra exhibit inactive motion, and a typical convection velocity for a large structure $c^+ \approx 15$ (or $0.75U_\infty$), one obtains a frequency $n^+ \approx 0.075$. In figure 16, the r.m.s. profiles corresponding to the Stokes solution at $n^+ = 0.05$ and $n^+ = 0.2$ are compared with the energy differences found in figure 13 between the cases $R_\theta = 1410$ and 670. All of the profiles are normalized to have the same slope at the wall (and therefore the same r.m.s. of the wall shear stress). The order-of-magnitude agreement seen in the figure lends support to a model based on the laminar Stokes solution with typical inactive-motion frequencies of the order of $n^+ = 0.1$. Bradshaw (1967) proposed a model based on small quasi-steady perturbations to the turbulent velocity profile. This model predicts for the inactive motion an r.m.s. proportional to $(U_0^+ + y^+ \mathrm{d}U_0^+/\mathrm{d}y^+)$, where $U_0^+(y^+)$ is the usual law of the wall. This quantity is also plotted in figure 16, with the

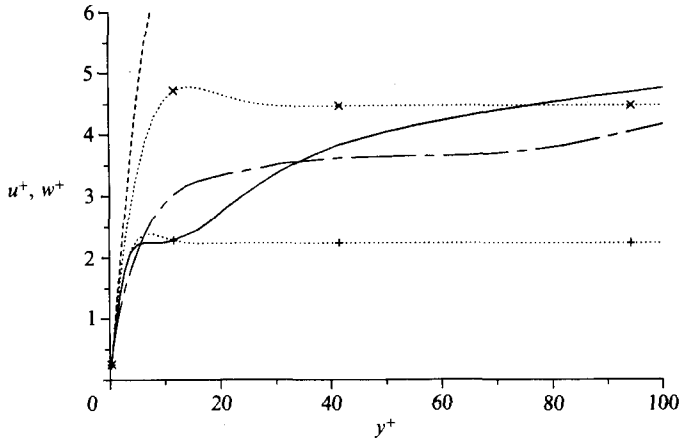

FIGURE 16. Profiles of inactive-motion r.m.s. Energy difference between $R_\theta = 670$ and 1410: ——, $\langle u^2 \rangle$; – – –, $\langle w^2 \rangle$. Stokes-layer model: +, $n^+ = 0.2$, ×, $n^+ = 0.05$. – · –, law-of-the-wall model.

same normalization, and is seen to be much larger than the other curves except very near the wall. This shows that the hypothesis (implicit in Bradshaw's model) that the velocity profile is in equilibrium with the wall shear stress is not satisfied at the present frequencies, except within a few wall units from the wall. The perturbed-law-of-the-wall model may supersede the laminar model but only at much higher Reynolds number, when sufficiently low frequencies n^+ carry the energy.

The behaviour of the Reynolds stresses will now be compared with the law given by Townsend (1976, p. 154) and Perry *et al.* (1985):

$$\langle u^2 \rangle^+ = B_1 - A_1 \log\left(\frac{y}{\delta}\right), \quad \langle w^2 \rangle^+ = B_2 - A_2 \log\left(\frac{y}{\delta}\right), \quad \langle v^2 \rangle^+ = A_3. \tag{11}$$

This law is thought to apply only in the fully turbulent region and at sufficiently high Reynolds numbers (as already mentioned, Perry *et al.* also proposed a viscous correction to extend this law to lower Reynolds numbers). The law implies that the stresses depend only on y/δ, which was well verified (after viscous correction, see figure 12). In contrast, at a fixed value of y^+ a term proportional to $\log(\delta u_\tau/\nu)$ enters the formula for $\langle u^2 \rangle$ and $\langle w^2 \rangle$ (but not $\langle v^2 \rangle$ or $\langle uv \rangle$). The results in figure 13 are quite consistent with this; notice the much smaller rise of $\langle v^2 \rangle$ (especially considering that r.m.s. values are shown; the convexity of the square-root function would enhance the variation of the v-intensity compared with the u- and w-intensities). Equation (11) predicts constant profiles in figure 16, which is consistent since it applies only outside the region affected by the no-slip condition.

Figure 17 shows another test of (11), comparing the y-dependence of the corrected $R_\theta = 1410$ results with the logarithmic behaviour predicted by (11), using $A_1 = 1.1$, $A_2 = 0.66$, $A_3 = 1.75$, $B_1 = 2.0$ and $B_2 = 1.1$. The first two values were chosen after inspection of the spectra (§3.4); the last three were chosen empirically. Perry *et al.* (1985) give slightly different values: $A_3 \approx 1.5$ to 1.9, $B_1 = 2.48$, $B_2 = 1.12$. The agreement in figure 17 is moderately good (recall that the wall region, $y^+ < 50, y/\delta < 0.075$, should be excluded, and that the slope of the straight lines was not adjusted to obtain the best agreement). Because of the insufficient Reynolds number, the present data cannot provide a definitive confirmation of (11), but they are consistent with it as shown in figures 12, 13 and 17.

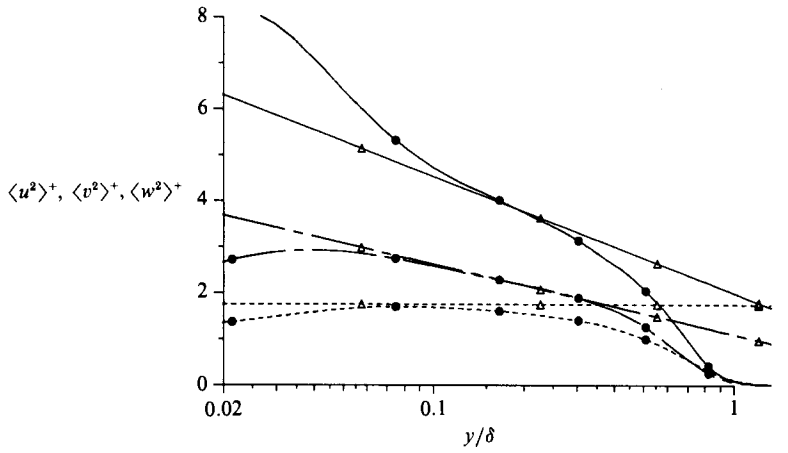

FIGURE 17. Reynolds stresses, extrapolated from $R_\theta = 1410$ to ∞. ——, $\langle u^2\rangle^+$; – – –, $\langle v^2\rangle^+$; ——, $\langle w^2\rangle^+$; ●, computed values; △, equation (11).

An unexpected implication of (11) is that at a given value of y^+, the stresses $\langle u^2\rangle^+$ and $\langle w^2\rangle^+$ not only depend on the Reynolds number, but even tend to ∞ like $\log(\delta^+)$ as the Reynolds number tends to ∞ (however, the log-layer overlap condition requires $\log(\delta^+) = U_\infty/u_\tau + B$, where B is a constant, so that $\langle u^2\rangle/U_\infty^2$ and $\langle w^2\rangle/U_\infty^2$ still tend to 0). Such a behaviour has not been indicated by experiments, but measurements in the wall layer at very high Reynolds numbers are difficult and may not be accurate enough to reveal a slow, logarithmic divergence. Direct simulations at Reynolds numbers higher than the present ones have not been conducted. Presumably, as the Reynolds number increases, the added energy will be independent of y^+ away from the wall and 'damped' by a factor similar to the ones in figure 16 near the wall. This damping will extend to higher values of y^+ as the frequency n^+ decreases so that the effect at a y^+ of 10, for instance, will be less than in the log layer. As a result, the shape of the Reynolds-stress profiles near the wall will be progressively altered; for instance the peak value of $\langle u^2\rangle^+$ will be displaced from its usual location into the log layer. In Klebanoff's (1954) measurements at $R_\theta \approx 7500$, the peak value of the r.m.s. of u^+ is about 2.98 and occurs at $y^+ \approx 22$. These values are significantly higher than the accepted values, which are about 2.7 and 13. Finally, note that the diagonal elements of the Reynolds-stress tensor can tend to ∞, compared with the off-diagonal elements, without violating the condition of realizability. The correlation coefficients simply tend to 0.

Another implication of the theory is that in (11) the constants B_1 and B_2 are not universal, so that the Reynolds stresses at a fixed y^+ depend not only on δ^+, but also on the type of flow: e.g. boundary-layer, pipe and channel (the definition of δ is also flow-dependent). Thus (11) conflicts in many ways with the concept of a law of the wall for the Reynolds stresses. Bradshaw (1967) used his quasi-steady perturbation model to show that the mean-velocity profile has very little sensitivity to the inactive motion, which could explain why it does not deviate appreciably from the law of the wall.

The flow structures at different Reynolds numbers were examined in relation with the failure of the law of the wall for some of the statistical quantities. Figures 18 and 19 show contours of constant vorticity magnitude at $R_\theta = 300$ and 1410, normalized by $(u_\tau^3/\delta\nu)^{\frac{1}{2}}$ (recall that this normalization yielded a collapse of the vorticity r.m.s. at

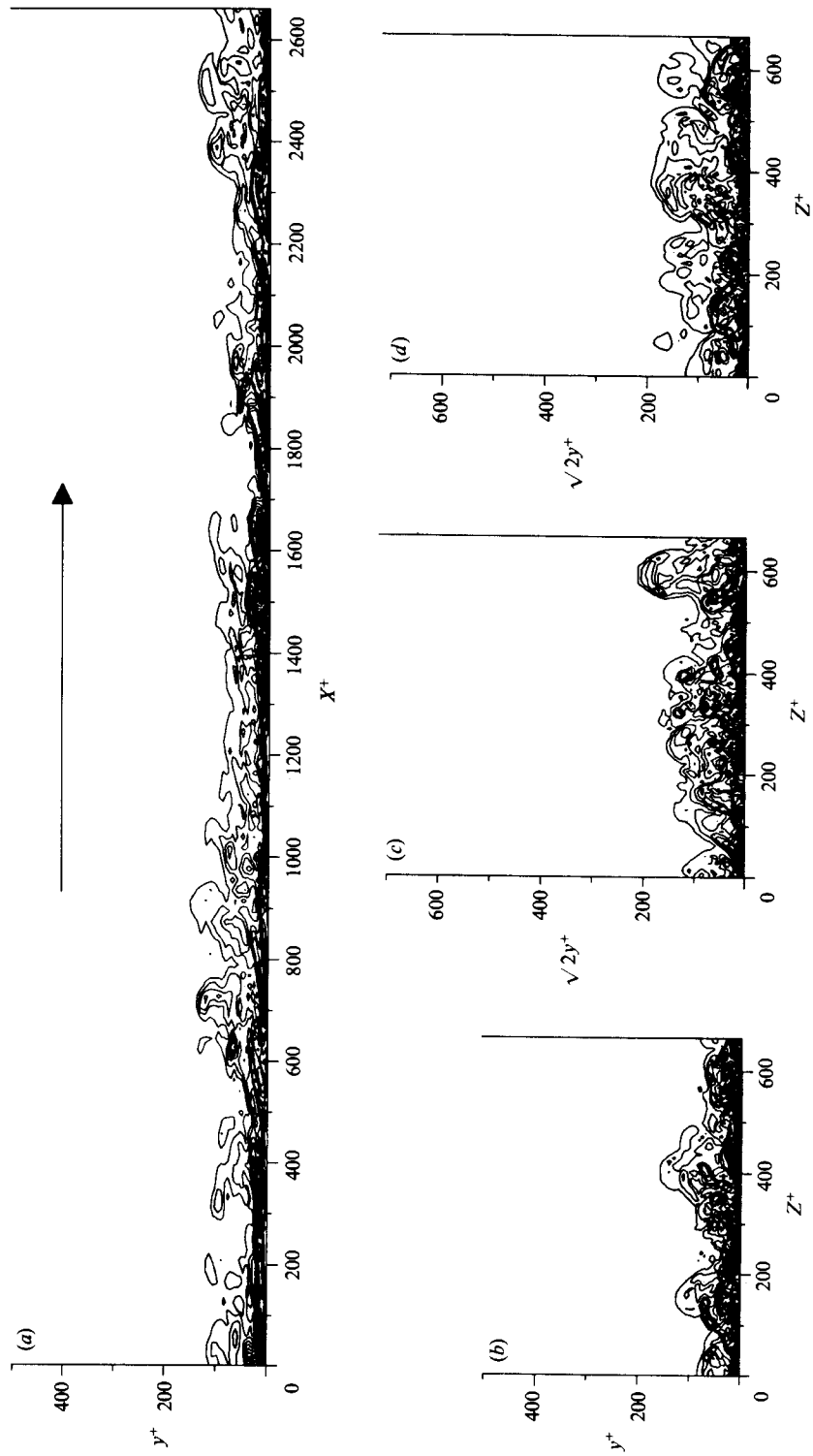

FIGURE 18. Vorticity contours, $R_\theta = 300$. (*a*) streamwise plane; (*b*) spanwise plane; (*c*) downstream plane, at 45°; (*d*) upstream plane, at 45°. Contour levels: $\|\omega\|[(\delta\nu/u_\tau^3)^{\frac{1}{2}} = 1, 2, 3, \ldots$.

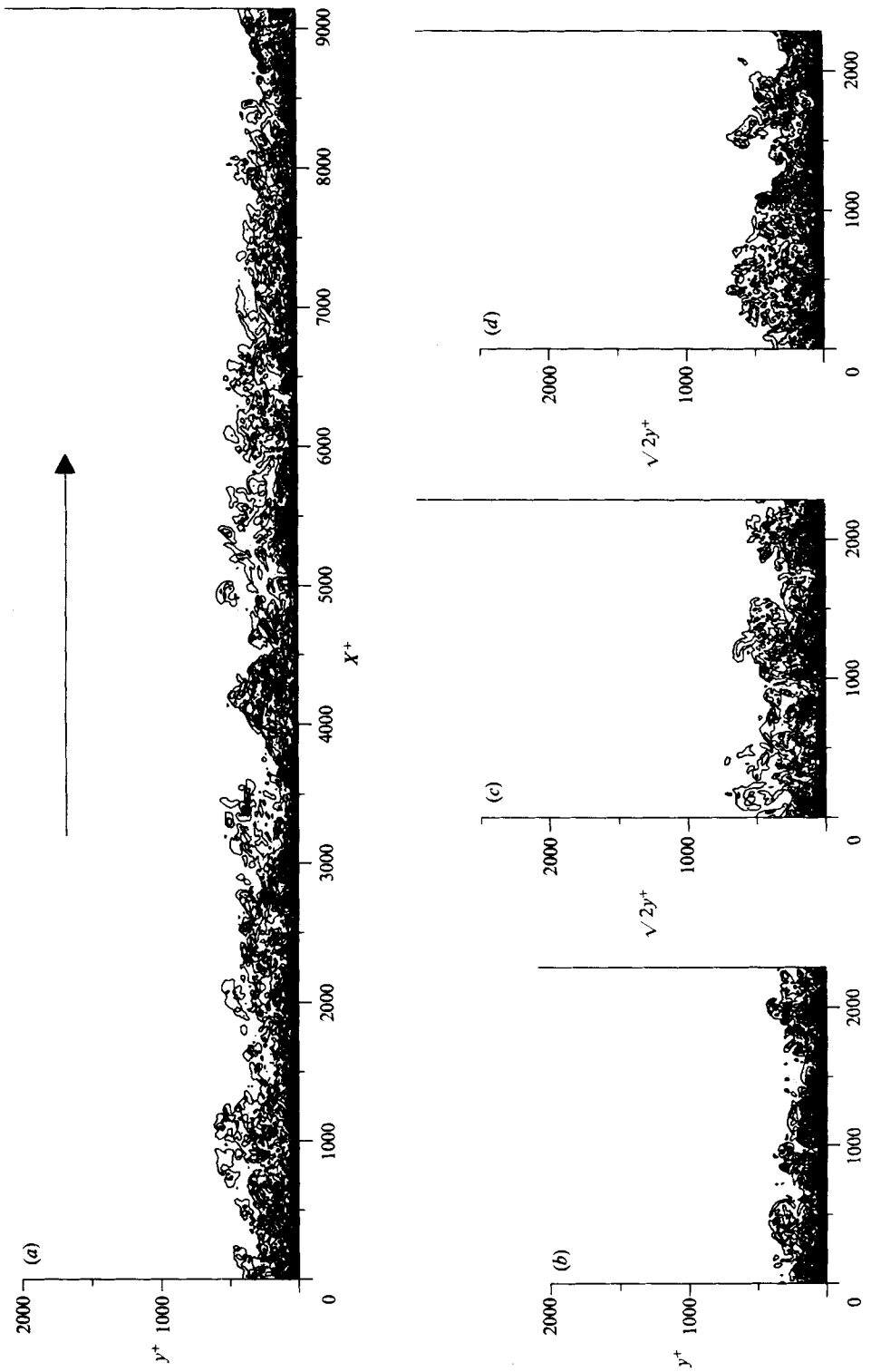

FIGURE 19. Vorticity contours, $R_\theta = 1410$. (*a*) streamwise plane; (*b*) spanwise plane; (*c*) downstream plane, at 45°; (*d*) upstream plane, at 45°. Contour levels: $\|\omega\| (\delta\nu/u_\tau^3)^{\frac{1}{2}} = 1, 2, 3, \ldots$.

different Reynolds numbers). Cross-sections of the flow by a streamwise plane, a vertical spanwise plane and oblique planes at $\pm 45°$ are taken in the manner of Falco (1977) and Head & Bandyopadhyay (1981). Similar figures were obtained from numerical simulations in channels (e.g. Deardorff 1970; Schumann 1975; Moin & Kim 1982). Note the depth of the irrotational 'valleys' and the sharpness of the irrotational–rotational interface (compared with the boundary-layer thickness), especially at the higher Reynolds number. This suggests that the entrainment process is at least qualitatively reproduced within the multiple-scale approximation (essentially because V is negative: $V \approx -0.025 U_\infty$ at $y = \delta$). Note also the absence of numerical oscillations in the irrotational region, as could be caused by inadequate resolution. The figures show that the 'typical eddies' are smaller (relative to the boundary-layer thickness) at higher Reynolds number, in agreement with experiments. There is some similarity between the present results and Head & Bandyopadhyay's smoke photographs, but the numerical results are far from being as convincing regarding the presence of hairpin vortices (except maybe the right end of figure 18*c* and the left end of figure 19*c*). It is also difficult to ascertain that the eddy scales in figures 18 and 19 are exactly the same in wall units, as Head & Bandyopadhyay's model implies. One possible problem with visualizing the numerical results is that the Navier–Stokes solver uses spectral interpolation, while the graphics program uses linear interpolation which is cruder.

3.4. *Analysis of the spectra*

The $R_\theta = 1410$ case is used for a more detailed study in order to minimize the low-Reynolds-number effects. In a wall-bounded flow, wavenumbers can be non-dimensionalized in at least four ways; one can use the Kolmogorov lengthscale $l_k \equiv (\nu^3/\epsilon)^{\frac{1}{4}}$, the wall lengthscale ν/u_τ, the distance from the wall y, or the thickness of the boundary layer, δ. The presentation of the results makes use of the different normalizations and owes much to Perry *et al.*'s work (1985, 1986). Their theory is based on certain assumptions about the shape of the eddies, and on dimensional analysis. Bradshaw (1967) also presented a theory based on dimensional analysis. Perry *et al.* tentatively define the 'fully turbulent region' by $y^+ > 100, y/\delta < 0.15$. Partly because of the moderate value of the Reynolds number, a less conservative definition was adopted here: $y^+ > 50, y/\delta < 0.3$.

Figure 20 shows spectra with Kolmogorov scaling. The maximum non-dimensional wavenumbers kl_k are about 0.3 and 0.8 in the x- and z-directions, respectively. The values of y^+ are 100 and 200 (recall that $\delta^+ \approx 660$). The spectra from the two planes collapse quite well for kl_k larger than about 0.05. Deviations appear at the highest wavenumbers, probably because of numerical truncation; there is even a slight turnup of the z-spectra. In the x-direction, the spectrum of $\langle u^2 \rangle$ has a significant inertial range, about half a decade. For the other components, the inertial ranges are insignificant. The Kolmogorov constant was computed as the maximum of $E(k)\, k^{\frac{5}{3}}$. As for the log layer, this definition has the advantage of being rigorous, but one should expect the Kolmogorov constants to be slightly overestimated especially if the spectra are noisy. The value for $\langle u^2 \rangle$ is 0.55 ± 0.05, which is in good agreement with the accepted value of about 0.5 (Townsend 1976). The transverse Kolmogorov constants are 0.62 and 0.7, with similar uncertainties, for $\langle v^2 \rangle$ and $\langle w^2 \rangle$, respectively. Recall that in isotropic turbulence, the transverse Kolmogorov constants are larger than the longitudinal one by a factor of $\frac{4}{3}$.

The behaviour of the z-spectra (figire 20*b*) is similar to the x-spectra for kl_k larger than 0.1, but for lower wavenumbers no inertial range is found. The spectra do not

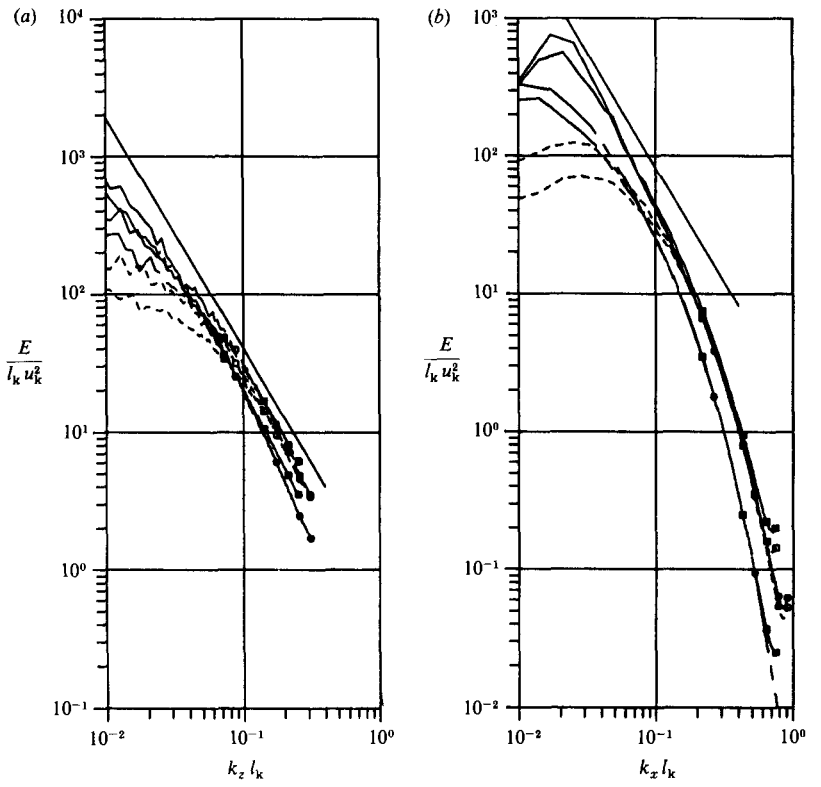

FIGURE 20. Spectra, Kolmogorov scaling. (*a*) *x*-direction; (*b*) *z*-direction. ——, $\langle u^2 \rangle$; – – –, $\langle v^2 \rangle$; – · –, $\langle w^2 \rangle$. □, $y^+ = 100$; ○, $y^+ = 200$.

remain tangent to a $k^{-\frac{5}{3}}$ law; instead they peel off for $k_z l_k$ lower than about 0.05. Furthermore, the Kolmogorov constants, defined as before, deviate from the accepted values more than in the *x*-direction: they are about 1.4, 0.7 and 0.6 for $\langle u^2 \rangle$, $\langle v^2 \rangle$ and $\langle w^2 \rangle$, respectively. It seems that a much higher Reynolds number is needed for the inertial-range behaviour to be set in the *z*-direction.

Figure 21 shows a test of the isotropy of the small scales. The one-dimensional spectra of an isotropic field satisfy $E_2 = E_3 = \frac{1}{2}(E_1 - k_1 \mathrm{d}E_1/\mathrm{d}k_1)$ where k_1 is the wavenumber, E_1 the spectral density in that direction and E_2 and E_3 the densities in the transverse directions (Townsend 1976). These three quantities are compared in figure 21, in the *z*-direction; the *x*-direction spectra show the same trend but are noisier. In figure 21 (*a*), with $y^+ = 200$, the small scales are seen to satisfy the isotropy conditions rather well for $k_1 l_k$ larger than about 0.1. In contrast, in figure 21 (*b*), with $y^+ = 40$, the spectra do not show isotropy. A similar test was conducted by Klebanoff (1954). The lack of isotropy of even the small scales near the wall is explained by the fact that the macroscales of the turbulence, namely y and ν/u_τ, are not much larger than the Kolmogorov scale l_k.

In theory, the spectra allow computation of the value of the constant C_1' (§3.3). As presented by Perry *et al.* (1985, 1986) the correction is $C_1/(y^+)^{\frac{1}{2}}$, $(\frac{4}{3})C_1/(y^+)^{\frac{1}{2}}$ and $(\frac{4}{3})C_1/(y^+)^{\frac{1}{2}}$ for $\langle u^2 \rangle^+$, $\langle v^2 \rangle^+$ and $\langle w^2 \rangle^+$, respectively. It seems disturbing that this correction is not isotropic. To obtain the $\frac{4}{3}$ factor, one needs to restrict one's attention to streamwise spectra, and to make the non-trivial assumption that the transverse spectral densities equal $\frac{4}{3}$ times the longitudinal spectral density even in the viscous

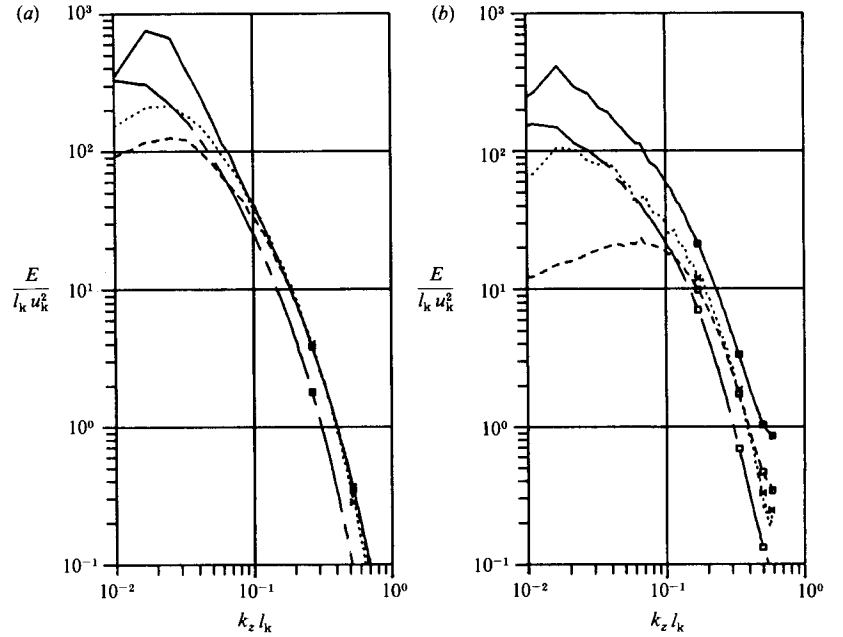

FIGURE 21. Spectra, Kolmogorov scaling, test of local isotropy. (*a*) $y^+ = 200$; (*b*) $y^+ = 40$. ——, $\langle u^2 \rangle$; – – –, $\langle v^2 \rangle$; — — —, $\langle w^2 \rangle$; ···, $\frac{1}{2}(E_1 - k_1 \mathrm{d}E_1/\mathrm{d}k_1)$.

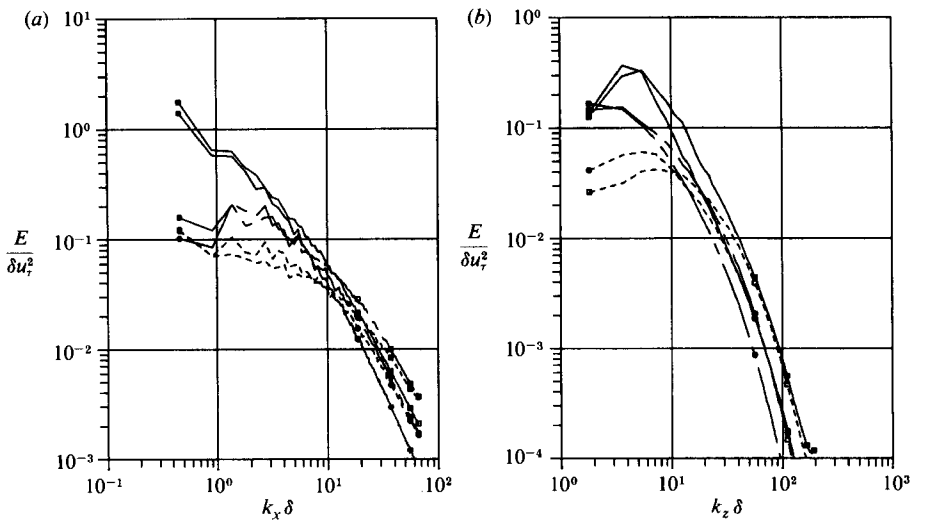

FIGURE 22. Spectra, normalized using δ. (*a*) x-direction; (*b*) z-direction. ——, $\langle u^2 \rangle$; – – –, $\langle v^2 \rangle$; — — —, $\langle w^2 \rangle$. □, $y^+ = 100$; ○, $y^+ = 200$.

peel-off range. This assumption is not compatible with the equation $E_2 = E_3 = \frac{1}{2}(E_1 - k_1 \mathrm{d}E_1/\mathrm{d}k_1)$ and the fact that in that range, $\mathrm{d}E_1/\mathrm{d}k_1 < (-\frac{5}{3})E_1/k_1$. In fact, using the isotropy equation, one can easily show that the integral is the same for the three velocity components. For the present study (including figure 12) it was decided to discard the $\frac{4}{3}$ factors.

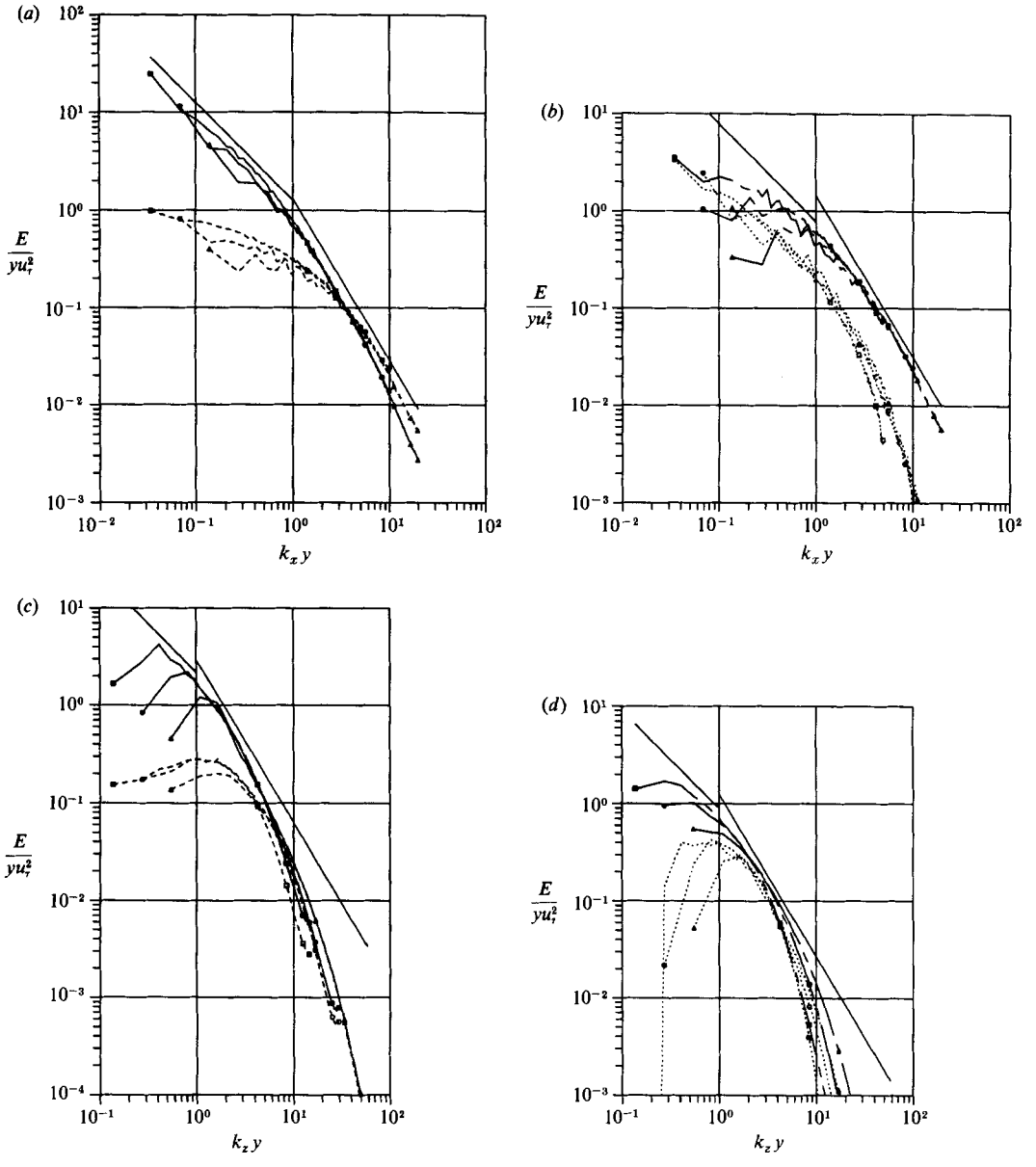

FIGURE 23. Spectra, normalized using y. (*a*), (*b*) x-direction; (*c*), (*d*) z-direction. ——, $\langle u^2 \rangle$; – – –, $\langle v^2 \rangle$; — · —, $\langle w^2 \rangle$; ···, $-\langle uv \rangle$. □, $y^+ = 50$; ○, $y^+ = 100$; △, $y^+ = 200$.

The values of the constants C_1 and C_1' are not easy to establish. They are related by $C_1 = C_1'/(\kappa)^{\frac{1}{2}}$ since in the constant-stress layer $\epsilon^+ = 1/(\kappa y^+)$. Perry *et al.* quote $C_1 = 6.08$, which implies $C_1' \approx 3.9$. They obtained this value by setting the spectrum to 0 beyond a peeloff wavenumber $kl_k = M$, which could yield a rather crude overestimate of the energy difference; M is also ill-defined. From the spectra in figure 20(*b*), one obtains the estimate $C_1' \approx 2$. However the spectra are thought to be somewhat inaccurate (too high) near the numerical cutoff, and the value of the Kolmogorov constant is not firmly established, so that this estimate is not very reliable either. To obtain a reliable estimate one would probably need a simulation

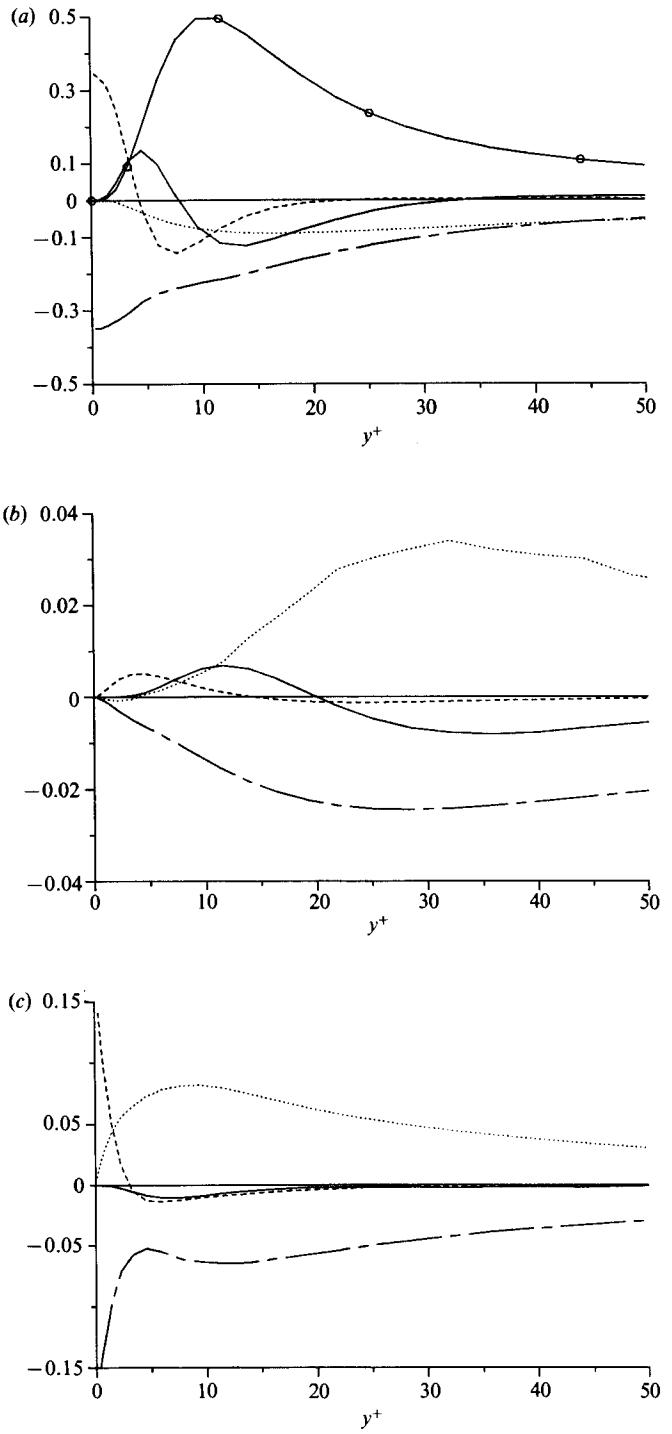

FIGURE 24 (*a–c*). For caption see facing page.

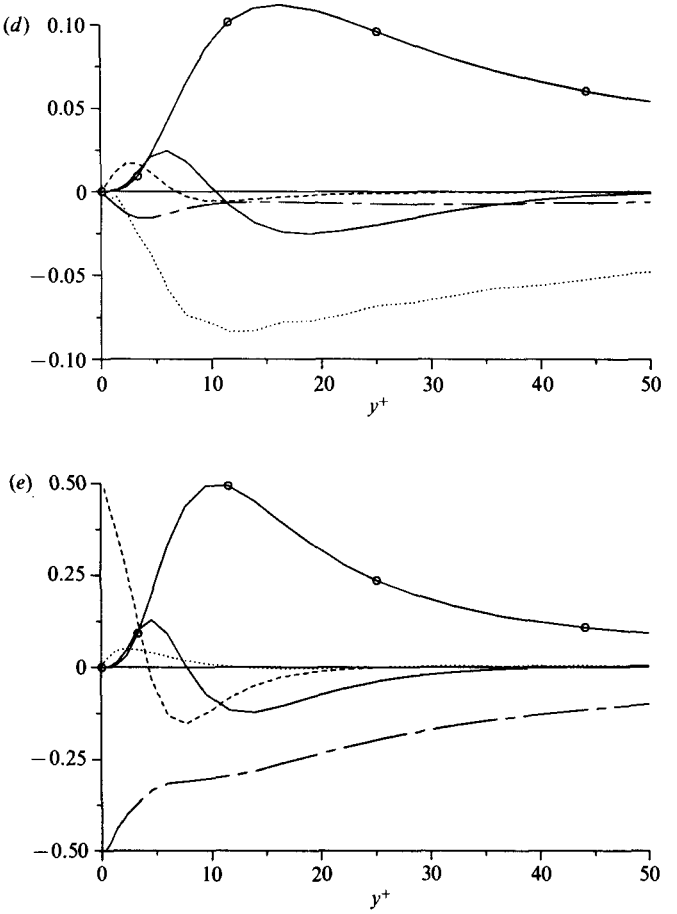

FIGURE 24. Reynolds-stress budget terms near wall. Normalized by u_τ^4/ν. (*a*) u^2; (*b*) v^2; (*c*) w^2; (*d*) $-uv$; (*e*) $u^2+v^2+w^2$. —○—, production; ——, turbulent diffusion; – – –, viscous diffusion; ——, dissipation; ···, pressure.

that exceeds the Kolmogorov wavenumber in all directions, and shows a convincing inertial range. Studies by Grant and Pao (see Hinze 1975) suggest values of about 5 and 3.4, respectively. The value $C_1' = 2.8 \pm 0.2$ was obtained empirically by optimizing the collapse of the profiles in figure 12.

In figure 22, δ is used as a lengthscale. Perry *et al.* (1985) predict that for low wavenumbers ($k_x\delta$ less than about 3), the spectra from different horizontal planes will collapse for u and w, but not v. Although the spectra are noisy especially at low wavenumbers, figure 22 shows encouraging agreement with the theory. The collapse is good for u in both directions and rather good for w. The v-spectra are higher for higher values of y, especially in the z-direction. The agreement with the experimental spectra of Bradshaw (1967) and Perry *et al.* (1985) is good for $k_x\delta$ larger than about 1. However for lower wavenumbers, the computed spectra do not level off like the experimental spectra. This is especially apparent for the spectra of u. Each set of data has its own sources of error. The experimenters converted frequency spectra into spatial spectra using Taylor's hypothesis, which is least valid for low wavenumbers (see Perry *et al.*'s discussion of the errors involved). The simulations directly yield spatial spectra, so these errors are avoided. On the other hand, the

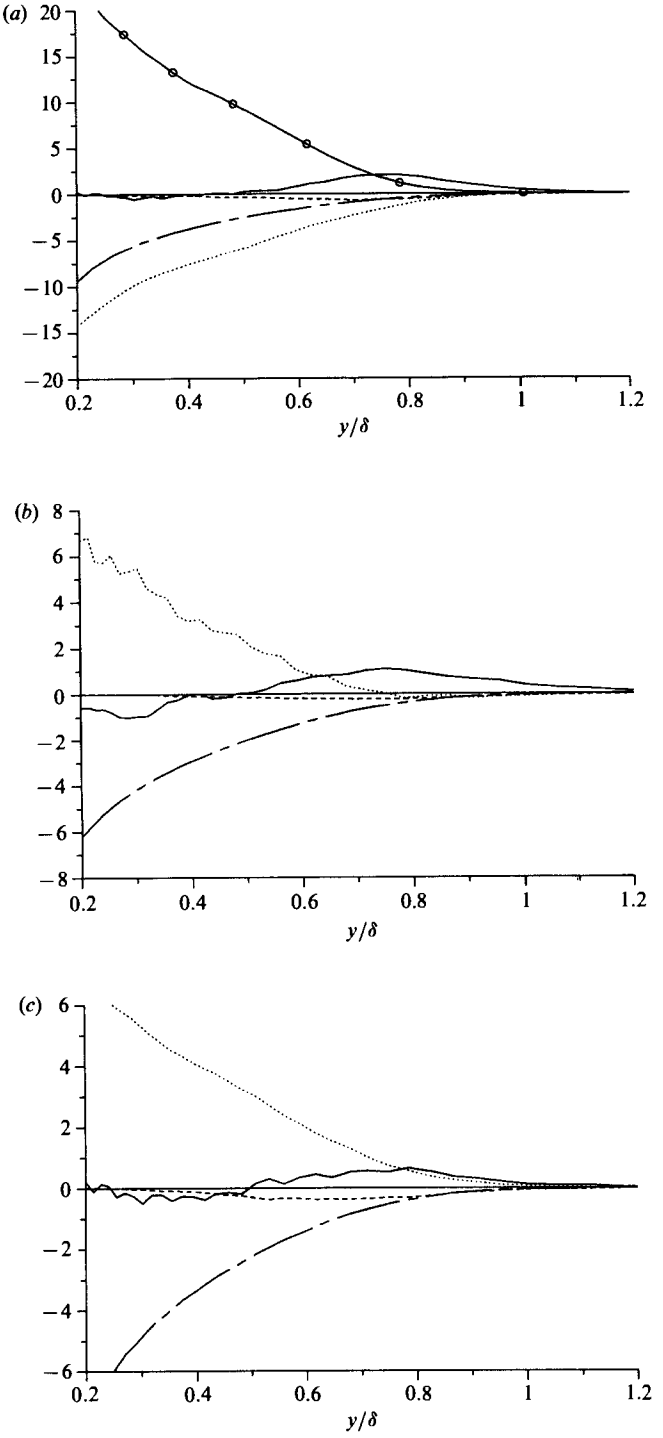

FIGURE 25(*a–c*). For caption see facing page.

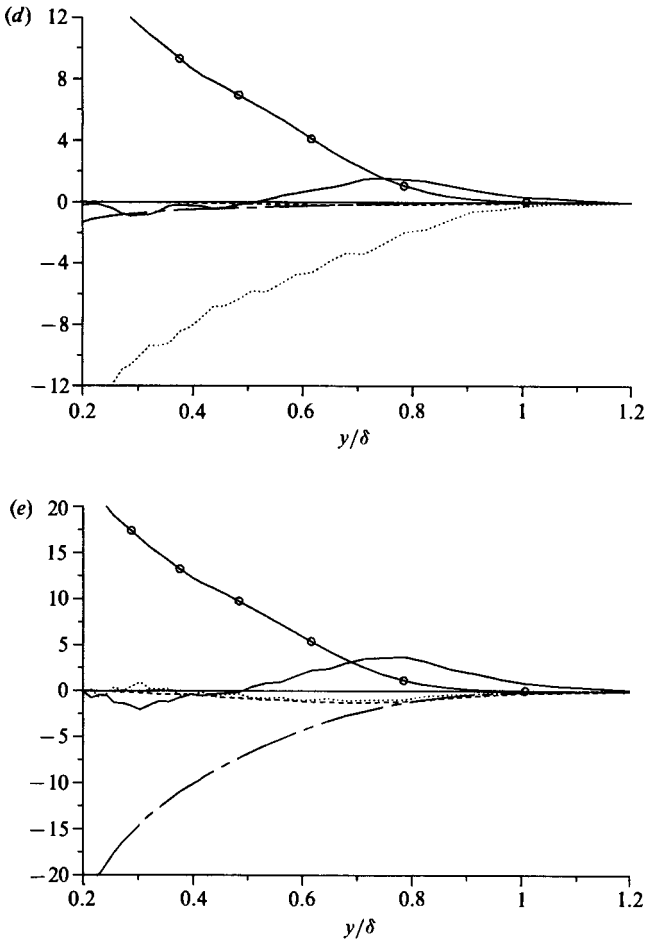

FIGURE 25. Reynolds-stress budget terms away from the wall. Normalized by u_τ^3/δ. (*a*) u^2; (*b*) v^2; (*c*) w^2; (*d*) $-uv$; (*e*) $u^2+v^2+w^2$. —○—, production; ——, turbulent diffusion; – – –, growth terms; – · – · –, dissipation; ···, pressure.

multiple-scale approximation may be showing its limitations here. In a true spatially-developing flow, the incoming flow has a smaller thickness and therefore the long waves are less energetic. Since this effect is suppressed by the approximations that were made one would expect the energy of the long waves to be slightly over-predicted, which is what the comparison between figure 22 and the experimental results suggests (the crude treatment of the straining effects, discussed in §2.2, could also play a role).

Finally figure 23 shows the spectra normalized with y as the lengthscale. This scaling provides the richest behaviour in Perry *et al.*'s (1985) theory: a collapse of spectra from different values of y, with a pivot point at $k_x y$ of the order of 1, a k_x^{-1} range on the left (except for v which is expected to be constant), and the $k_x^{-\frac{5}{3}}$ range on the right. Experimental results generally confirm this picture (Klebanoff 1954; Perry *et al.* 1985). In figure 23, segments with slope -1 and $-\frac{5}{3}$ are tentatively drawn on all the plots. In the x-direction, the results show a good collapse on the right of the pivot, with the curves corresponding to lower values of y peeling off first. The degree of agreement with a $k^{-\frac{5}{3}}$ law was discussed earlier. In the z-direction the

collapse, like the $k^{-\frac{5}{3}}$ behaviour, may be prevented by the insufficient range of scales. However, there is no reason why the theory should not apply to spanwise spectra.

On the left of the pivot, the collapse and the agreement with the k^{-1} model are convincing only for $\langle u^2 \rangle$ and $\langle -uv \rangle$, in the x-direction. A conclusive check of the theory is made difficult by the statistical noise, the finite values of the periods Λ_x and Λ_z, and the limited range of scales due to the moderate value of the Reynolds number. From figure 23 one can estimate the constants multiplying k_x^{-1} for the various components. For $\langle -uv \rangle$, it is 0.18, which is in excellent agreement with Klebanoff's (1954) measurements. Using Perry *et al.*'s notation, the computed values (which are probably slightly overestimated) are: for u, $A_1 = 1.1$; for w, $A_2 = 0.66$. These constants entered (11) (in fact (11) is a direct consequence of the existence of a k^{-1} range). Perry *et al.* (1985, note that their values are switched in their table 1) quote $A_1 = 1.03$, $A_2 = 0.73$. In a pipe flow Perry *et al.* (1986) measured $A_1 = 0.90$; Klebanoff (1954) obtained $A_1 \approx 0.85$. These constants are thought to be universal. The agreement between measured and computed values is acceptable.

3.5. *Reynolds-stress budget equations*

The various terms in the budget of the four non-zero Reynolds stresses are shown in figure 24, near the wall, and in figure 25 away from the wall. The contribution of the growth (or advection) terms is negligible near the wall (recall that V is zero in that region) and becomes noticeable only for y/δ larger than about 0.5. Conversely, the viscous diffusion is negligible for $y^+ > 25$. The terms sum up to 0 very well near the wall; in the outer region the residuals are less than 0.5 in the units of figure 25. As expected the near-wall behaviour is similar to that observed in a channel flow (Moser & Moin 1984). As the Reynolds number increases, there is a weak trend for most of the quantities in figure 24 to increase. Furthermore, there is a very noticeable enhancement (up to 20% increase from $R_\theta = 300$ to 1410) of the dissipation and of the viscous diffusion for y^+ smaller than about 10 (as part of the inactive-motion theory Bradshaw (1967) predicted that the dissipation and the turbulent diffusion would be enhanced). Since the inactive motion has long timescales, one expects it to contribute relatively less to the energy budget than to the energy itself. The enhancement of the viscous diffusion is of course linked to the increase of the Reynolds stresses, seen in figure 13. The profiles in figure 24 should be considered as representative, but not as universal.

In figure 25 the terms are normalized by u_τ^3/δ. Again, one should not take the results as universal. At higher Reynolds numbers the dissipation tensor slowly becomes more isotropic. This evolution of the dissipation terms is compensated for by the pressure terms and the turbulent-diffusion terms, in roughly equal parts. Note that numerical truncation, by suppressing small-scale structures, tends to artificially increase the anisotropy of the dissipation tensor; the refined simulation that was done at $R_{\delta^*} = 500$ showed slightly less dissipation-tensor anisotropy than the basic simulation. For the shear stress, the production and pressure terms both increase significantly with Reynolds number. Thus unless it explicitly includes low-Reynolds-number effects, a turbulence model should not be expected to match the present results very closely. For the total energy, the production and the dissipation are in balance over most of the boundary layer; but for separate components, the pressure term is often significant. For y/δ between about 0.5 and 1.2, the turbulent-diffusion and growth terms become important. In this flow the contribution of the growth terms to the Reynolds-stress budget is consistently negative.

4. Conclusions

Direct numerical simulations of the turbulent boundary layer on a flat plate were performed at four Reynolds numbers, including a value significantly larger than in any previous direct simulations. A systematic multiple-scale procedure was used to approximate the local effects of the streamwise growth of the flow. The numerical truncation errors were shown to be much smaller than the relevant variations of the results. In general the agreement with experimental results was good. The most significant discrepancy is in the friction coefficient at the highest Reynolds number; the computed value is too large by about 5%.

The mean-velocity and shear-stress profiles behaved as predicted by Coles, except for the strength of the wake. At very low Reynolds numbers, R_θ less than about 600, the logarithmic layer disappears, and the Clauser-plot method yields incorrectly high values of the friction velocity. A definition of the boundary-layer thickness δ as an integral of the total shear stress was introduced, and produced a very good collapse of the stress profiles from different Reynolds numbers. The total stress appears to approach the wall with a finite slope, in contrast with the parabolic behaviour that is usually assumed. The other Reynolds stresses also collapsed very well, away from the wall, after a variant of Perry's viscous correction was applied. When the boundary-layer thickness δ is used as a length scale, the energy of the small-scale motion increases with Reynolds number.

The main result of the paper is that near the wall the normal Reynolds stresses $\langle u^2 \rangle$ and $\langle w^2 \rangle$, unlike the mean velocity and the shear stress, do not collapse when normalized with ν and u_τ. The pressure and vorticity intensities do not collapse either. Instead, they all show a strong tendency to increase with Reynolds number, consistent with Townsend and Perry's theories. The lack of collapse extends all the way to the wall. The theories even predict that the stresses at fixed y^+ tend to infinity like the logarithm of the outer-flow Reynolds number, and that they depend on the type of outer flow. When the wall lengthscale ν/u_τ is used, the large-scale motion is responsible for the increased energy. The waves fit the description of 'inactive motion' given by Townsend and Bradshaw. A simple model based on an oscillating near-wall layer predicted the proper trend for the stress variation with Reynolds number, but a convincing quantitative extension of the theories into the wall region remains to be found.

The spectra showed encouraging agreement with various theories, including Kolmogorov's and Perry's, and yielded satisfactory values for most of the universal constants. Extensive data were provided for the development of turbulence models both near the wall and in the outer region, and the Reynolds-number dependence of the major terms was discussed. The anisotropy of the dissipation tensor was found to be significant even at the highest Reynolds number reached.

The author had useful discussions with Drs J. Kim, N. Mansour, P. Moin, R. Rogallo and A. Wray (NASA Ames Research Center), and with Professor P. Bradshaw (Imperial College, London). Dr Mansour reviewed the manuscript.

Appendix

We examine the classical two-layer model of the flat-plate turbulent boundary layer (Townsend 1956, p. 229), especially the local momentum equation. The assumptions are, near the wall:

$$U^+ = f(y^+), \quad \tau^+ = 1, \tag{A 1a,b}$$

and away from the wall:

$$(U - U_\infty)^+ = g\left(\frac{y}{\delta}\right), \quad \tau^+ = h\left(\frac{y}{\delta}\right), \tag{A 2a,b}$$

for some non-dimensional functions f, g and h. The boundary-layer momentum and continuity equations are

$$UU_x + VU_y = \frac{\partial \tau}{\partial y}, \quad U_x + V_y = 0. \tag{A 3}$$

In the wall region, which includes the log layer, the momentum equation becomes (after some algebra and using continuity):

$$h' = \frac{\delta u_{\tau x}}{u_\tau} f^2. \tag{A 4}$$

Strictly speaking this contradicts (A 2b), because the right-hand side of (A 4) is not just a function of y/δ. Is it compatible with a parabolic behaviour of g, in particular as the Reynolds number tends to ∞? When this happens $\delta u_{\tau x}/u_\tau$ tends to 0 and f^2 tends to ∞ (at fixed y/δ); we therefore need better estimates. We shall use the overlap condition and the total-momentum equation.

Equations (A 1a) and (A 2a) overlap in the log layer. By differentiating the overlap condition with respect to x, we obtain (Coles 1956)

$$\frac{\delta_x}{\delta} + \frac{u_{\tau x}}{u_\tau}\left(1 + \kappa \frac{U_\infty}{u_\tau}\right) = 0. \tag{A 5}$$

The total-momentum equation is $\mathrm{d}\theta/\mathrm{d}x = u_\tau^2/U_\infty^2$. Using (A 1$a$) and (A 2$a$) we obtain

$$\theta = D_1 \frac{u_\tau}{U_\infty}\delta + D_2 \frac{u_\tau^2}{U_\infty^2}\delta + D_3 \frac{\nu}{U_\infty} + D_4 \frac{\nu u_\tau}{U_\infty^2} \tag{A 6}$$

for some constants $D_1 \approx 3.9$, $D_2 \approx -24$, $D_3 \approx 52$ and D_4. Clauser (1954) gives the value 3.6 for D_1 (Δ in his notation).

We compute $\mathrm{d}\theta/\mathrm{d}x$, neglecting the last term in (A 6) which is very small, and using (A 5) to eliminate δ_x:

$$\frac{\delta u_{\tau x}}{u_\tau}\left[-\kappa D_1 + (1-\kappa)\frac{D_2 u_\tau}{U_\infty}\right] = \frac{u_\tau^2}{U_\infty^2}, \tag{A 7}$$

so that (A 4) becomes

$$h' = -\frac{1}{\left(\kappa D_1 - (1-\kappa)\dfrac{D_2 u_\tau}{U_\infty}\right)}\left(\frac{U^2}{U_\infty^2}\right). \tag{A 8}$$

We consider a fixed value of y/δ (but within the log layer) and let the Reynolds number tend to ∞. The ratio u_τ/U_∞ tends to 0 and U/U_∞ tends to 1. Therefore the leading term is $-1/(\kappa D_1)(\approx -0.6)$ and is a constant. This means that up to the edge of the log layer $\tau^+(y)$ has a flat part with finite slope $-0.6/\delta$. Townsend (p. 255, 1956

edition) obtains the same behaviour, with slope about -0.5. Curiously, he removed this result for the 1976 edition. Li *et al.* (1986) also obtained (A 8); they outline a derivation which is most probably equivalent to the one given here. At moderate Reynolds numbers, both factors in (A 8) get smaller. Klebanoff's 1954 results and the present results show about -0.5 for h' up to $y/\delta \approx 0.2$.

REFERENCES

BANDYOPADHYAY, P. R. 1987 Resonant flow in a row of small transverse cavities submerged in a turbulent boundary layer. *AIAA*-87-1235.

BRADSHAW, P. 1967 'Inactive' motion and pressure fluctuations in turbulent boundary layers. *J. Fluid Mech.* **30**, 241–258.

CLAUSER, F. 1954 Turbulent boundary layers in adverse pressure gradients. *J. Aero. Sci.* **21**, 91–108.

COLES, D. E. 1956 The law of the wake in the turbulent boundary layer. *J. Fluid Mech.* **1**, 191–226.

COLES, D. E. 1962 The turbulent boundary layer in a compressible fluid. *Rand. Rep.* R403-PR, ARC 24473: Appendix A: A manual of experimental practice for low-speed flow.

COLES, D. E. 1978 A model for flow in the viscous sublayer. *Workshop on Coherent Structures of Turbulent Boundary Layers, AFOSR/Lehigh University, Bethlehem, PA.*, pp. 462–475.

DEARDORFF, J. W. 1970 A numerical study of three-dimensional turbulent channel flow at large Reynolds numbers. *J. Fluid Mech.* **41**, 453–480.

ERM, L. P., SMITS, A. J. & JOUBERT, P. N. 1985 Low Reynolds number turbulent boundary layers on a smooth flat surface in a zero pressure gradient. *Proc. 5th Symp. on Turbulent Shear Flows, Ithaca, NY, August 7–9, 1985.*

FALCO, R. E. 1977 Coherent motions in the outer region of turbulent boundary layers. *Phys. Fluids Suppl.* **20**, 124–132.

HEAD, M. R. & BANDYOPADHYAY, P. 1981 New aspects of turbulent boundary layer structures. *J. Fluid Mech.* **107**, 297–338.

HINZE, J. O. 1975 *Turbulence*. 2nd edn. McGraw-Hill.

KIM, H. T., KLINE, S. J. & REYNOLDS, W. C. 1968 An experimental study of turbulence production near a smooth wall in a turbulent boundary layer with zero pressure gradient. *Report* MD-20, Stanford University, CA.

KLEBANOFF, P. S. 1954 Characteristics of turbulence in a boundary layer with zero pressure gradient. *NACA* TN-3178.

LI, J. D., HENBEST, S. M. & PERRY, A. E. 1986 The difficulties in the measurements of Reynolds stresses in smooth- and rough-wall turbulent boundary layers. *Proc. 9th Australasian Fluid Mechanics Conf., Auckland, New Zealand, Dec. 8–12, 1986.*

MOIN, P. & KIM, J. 1982 Numerical investigation of turbulent channel flow. *J. Fluid Mech.* **118**, 341–377.

MOSER, R. D. & MOIN, P. 1984 Direct numerical simulation of curved turbulent channel flow. *NASA* TM-85974. Also 1987 *J. Fluid Mech.* **175**, 479.

MURLIS, J., TSAI, H. M. & BRADSHAW, P. 1982 The structure of turbulent boundary layers at low Reynolds numbers. *J. Fluid Mech.* **122**, 13–56.

PELZ, R. B., YAKHOT, V., ORSZAG, S. A., SHTILMAN, L. & LEVICH, E. 1985 Velocity-vorticity patterns in turbulent flow. *Phys. Rev. Lett.* **54**, 2505.

PERRY, A. E., LIM, K. L. & HENBEST, S. M. 1985 A spectral analysis of smooth flat-plate boundary layers. *Proc. 5th Symp. on Turbulent Shear Flows, Ithaca, NY, August 7–9, 1985.*

PERRY, A. E., HENBEST, S. & CHONG, M. S. 1986 A theoretical and experimental study of wall turbulence. *J. Fluid Mech.* **165**, 163–199.

PRESTON, J. H. 1957 The minimum Reynolds number for a turbulent boundary layer and the selection of a transition device. *J. Fluid Mech.* **3**, 373–384.

PURTELL, L. P., KLEBANOFF, P. S. & BUCKLEY, F. T. 1981 Turbulent boundary layers at low Reynolds numbers. *Phys. Fluids* **24**, 802–811.

ROGALLO, R. S. 1981 Numerical experiments in homogeneous turbulence. *NASA* TM-81315.

ROGALLO, R. S. & MOIN, P. 1984 Numerical simulation of turbulent flows. *Ann. Rev. Fluid Mech.* **16**, 99–138.

SCHEWE, G. 1983 On the structure and resolution of wall-pressure fluctuations associated with turbulent boundary-layer flow. *J. Fluid Mech.* **134**, 311–328.

SCHLICHTING, H. 1979 *Boundary Layer Theory.* 7th edn. McGraw-Hill.

SCHUMANN, U. 1975 Subgrid scale models for finite difference simulations of turbulent flows in plane channels and annuli. *J. Comp. Phys.* **18**, 376–404.

SIMPSON, R. L. 1970 Characteristics of turbulent boundary layers at low Reynolds numbers with and without transpiration. *J. Fluid Mech.* **42**, 769–802.

SPALART, P. R. 1986*a* Numerical simulation of boundary layers: Part 1. Weak formulation and numerical method. *NASA* TM-88222.

SPALART, P. R. 1986*b* Numerical study of sink-flow boundary layers. *J. Fluid Mech.* **172**, 307–328.

SPALART, P. R. & LEONARD, A. 1985 Direct numerical simulation of equilibrium turbulent boundary layers. *Proc. 5th Symp. on Turbulent Shear Flows, Ithaca, NY, August 7–9, 1985* (bound volume, 234).

TOWNSEND, A. A. 1956 *The Structure of Turbulent Shear Flow*, 1st edn. Cambridge University Press.

TOWNSEND, A. A. 1961 Equilibrium layers and wall turbulence. *J. Fluid Mech.* **11**, 97–120.

TOWNSEND, A. A. 1976 *The Structure of Turbulent Shear Flow*, 2nd edn. Cambridge University Press.

WILLMARTH, W. W. 1975 Pressure fluctuations beneath turbulent boundary layers. *Ann. Rev. Fluid Mech.* **7**, 13–38.

WRAY, A. A. 1987 Minimal storage time-advancement schemes for spectral methods. *J. Comp. Phys.* (in press).